Research Square

Preprints are preliminary reports that have not undergone peer review.
They should not be considered conclusive, used to inform clinical practice,
or referenced by the media as validated information.

Imaging magma ascent and discharge during the 2020-2022 paroxysmal activity at Mount Etna from geodetic data

Alejandra Vásquez Castillo
alejandra.vasquez@ingv.it
Istituto Nazionale di Geofisica e Volcanologia
Francesco Guglielmino
Istituto Nazionale di Geofisica e Volcanologia
Giuseppe Puglisi
Istituto Nazionale di Geofisica e Volcanologia
Alessandro Bonforte
Istituto Nazionale di Geofisica e Volcanologia

Research Article

Keywords: Volcano geodesy, Mount Etna, InSAR, GNSS, 3D surface deformation

Posted Date: April 20th, 2026

DOI: https://doi.org/10.21203/rs.3.rs-9316552/v1

License: This work is licensed under a Creative Commons Attribution 4.0 International License.
Read Full License

Additional Declarations: No competing interests reported.

Research Article

Imaging magma ascent and discharge during the 2020-2022 paroxysmal activity at Mount Etna from geodetic data

Alejandra Vásquez Castillo[1,2] ✉ · Francesco Guglielmino[1] · Giuseppe Puglisi[1] · Alessandro Bonforte[1]

[1] Istituto Nazionale di Geofisica e Vulcanologia - Osservatorio Etneo, Sezione di Catania, Italy
[2] Dipartimento di Scienze Biologiche, Geologiche e Ambientali – Sezione di Scienze della Terra, Università degli Studi di Catania, Catania, Italy
✉ **alejandra.vasquez@ingv.it**

Abstract

Mount Etna has shown persistent summit activity in recent decades, with the South-East Crater producing frequent lava fountains and explosive events. A phase of intense paroxysms began in December 2020, preceding two major paroxysmal sequences that lasted until February 2022, with 17 events in the first sequence (February–March 2021) and 33 in the second (concentrated predominantly between May–August 2021). To investigate the processes driving this activity, we analysed ground deformation recorded by Global Navigation Satellite System (GNSS) and Interferometric Synthetic Aperture Radar (InSAR) between January 2020 and February 2022. The pre-paroxysmal period exhibits a composite deformation field dominated by the eastward acceleration of the eastern flank and accompanied by deep (20–30 km) and intermediate-depth seismicity that we interpret as evidence of repeated magma injections. Our modelling identifies two distinct pre-paroxysmal phases marked by upward migration of pressurised sources from ~5.5 km to ~4.2 km depth. During the paroxysmal sequences, Etna exhibited pronounced centripetal deflation centred on the summit. Sequence 1 produced strong, volcano-wide deformation driven by rapid magma withdrawal from a shallow reservoir. Sequence 2 showed weaker but more complex deformation, reflecting overlapping contributions from shallow magma input, crystallisation, volatile exsolution and persistent flank slip. The temporal alignment between deep seismicity, compositional shifts towards more primitive magmas and geodetic source migration indicates a vertically stratified and dynamically connected plumbing system. Our results show that Etna's 2020–2022 paroxysmal cycle was driven by stepwise magma ascent from deep reservoirs to shallow levels, strongly modulated by flank kinematics and evolving storage conditions.

Keywords Volcano geodesy · Mount Etna · InSAR · GNSS · 3D surface deformation

Acknowledgments

The authors thank the INGV technical group for maintaining the GNSS network. We are grateful to P. De Gori for supplying seismic tomography data, and to R. Corsaro for providing petrological data and for the fruitful discussions. We produced maps using PyGMT (Tian et al., 2024) and acknowledge Flavio Cannavò and Yunjun Zhang for developing the GAME and MintPy software packages, respectively.

Funding

This research has received funding from the European Union's Horizon 2020 research and innovation programme through the IMPROVE project under grant agreement No 858092.

Conflicts of interest/Competing interests

The authors declare no competing interests.

Availability of data and material

The Sentinel-1 SAR images were obtained from the Alaska Satellite Facility archive (https://asf.alaska.edu). The original Copernicus Sentinel-1 data are owned by the European Space Agency.

Introduction

Ground deformation in volcanic regions records the surface expression of subsurface magmatic processes such as magma migration, reservoir pressurisation, dyke intrusion as well as the structural response of the volcanic edifice (Dzurisin, 2006; Biggs et al., 2014; Freymueller et al., 2015). However, the interpretation of surface deformation at active volcanoes is complex as an interplay of multiple processes at different depths and timescales produce overlapping signals that are difficult to isolate. This complexity increases at open-conduit systems where shallow magma withdrawal, deep recharge and flank dynamics interact continuously (Neri and Acocella, 2006), making the isolation of individual source contributions scientifically challenging and critical for eruption forecasting, risk assessment and hazard mitigation (Neri et al., 2009; Bonaccorso et al., 2021).

Mount Etna, rising to approximately 3400 m a.s.l. (De Beni et al., 2026) on the eastern coast of Sicily, is Europe's most active volcano and one of the most extensively monitored volcanic systems in the world. Its volcanic activity is characterised by the alternation of effusive and explosive activity from its active summit craters as well as by the occurrence of flank eruptions (Acocella & Neri, 2003). The current structure of the summit region consists of four craters: Voragine Crater (VC), documented as the oldest crater, North-East Crater (NEC), formed in 1911, Bocca Nuova Crater, with formation registration from 1968, and the South-East Crater (SEC), formed in 1971 (Branca & Del Carlo, 2004), which has been the most active one in the last decades (Andronico et al., 2021). In 2006, a new vent opened on the southeastern flank of SEC, which concentrated the volcanic activity for about a decade, forming a new morphologically distinct pyroclastic cone called the New South-East Crater (NSEC, Acocella et al., 2016). Due to the continuous activity of SEC and NSEC the two cones merged so that since November 2020, INGV identifies the whole structure as SEC (Andronico et al., 2021).

Paroxysmal activity, characterised by Strombolian explosions, lava fountaining, ash emissions, occasionally rapid lava effusion, and generally lasting no more than a few hours (Corsaro et al., 2017) is one of the signature features of the recent eruptive behaviour of Mt. Etna and its frequency has increased since the mid-1960s (Acocella et al., 2016). While in earlier periods the occurrence of paroxysms was limited to one or two episodes per decade, the past two decades have seen a significant rise in their frequency (Behncke and Neri, 2003; Acocella et al., 2016). Since 2011, this type of activity has concentrated at the SEC, with remarkable sequences occurring in 2011–2012 (25 episodes), 2013 (18 episodes), and at the VOR crater in 2015 and 2016 (four and three episodes,

respectively; Andronico et al., 2015; Bonaccorso et al., 2013; Bonaccorso et al., 2014; Bonaccorso & Calvari, 2017; Bonforte et al. 2021; Cannata et al., 2018; Spampinato et al., 2015).

Before the onset of intense paroxysmal activity in late 2020, Mount Etna experienced a period of continuous inflation following the December 2018 flank eruption (Bruno et al., 2022), the most recent flank eruption at Etna, which opened an eruptive fissure at the base of the SEC along a southeast trend, feeding lava flows into the Valle del Bove (Bonforte et al., 2019; Cannavò et al., 2019; Calvari et al., 2020; Mattia et al., 2020). This inflationary trend was interrupted by intense Strombolian activity in April 2020 (Bruno et al., 2022; Calvari et al., 2022; Giuffrida et al., 2023), before the summit craters showed vigorous activity and increasing seismicity in the final months of 2020, marking the beginning of one of the most remarkable paroxysmal cycles in Etna's recent history.

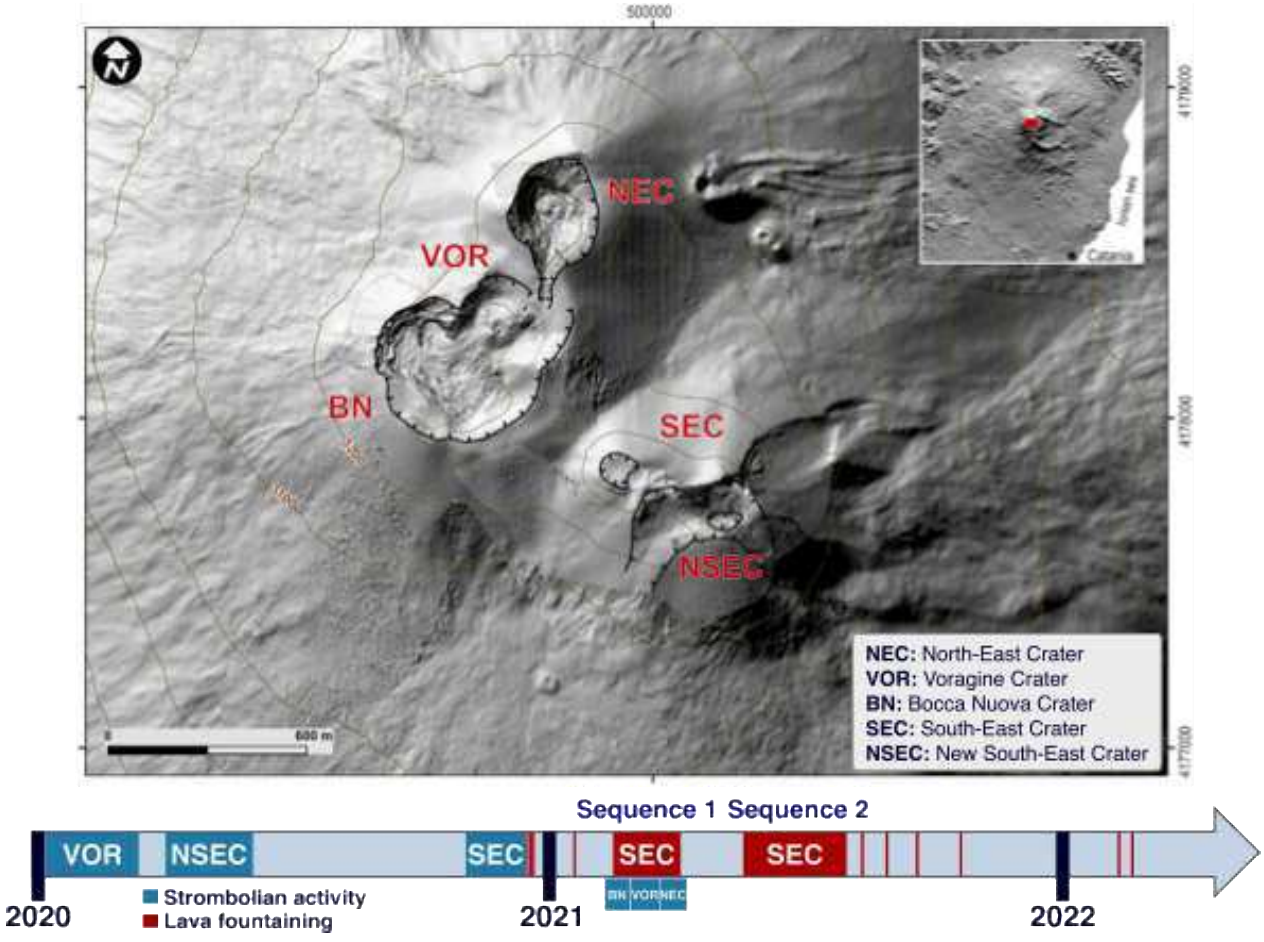


Fig. 1 Top: DEM of Etna's summit area highlighting the main craters (modified from Corsaro et al., 2022). Bottom: Timeline of the paroxysmal activity between 2020 and 2022. Strombolian activity is highlighted in blue, the paroxysmal episodes in red. The craters involved in the paroxysmal activity are indicated. The two paroxysmal sequences are marked as Sequence 1 and Sequence 2. Data from Calvari and Nunnari (2022)

A period of paroxysms began in December 2020 with the occurrence of four eruptive episodes and intensified in February 2021 (Fig. 1), lasting until the end of March 2021 (hereafter SEQ1, following the nomenclature of Corsaro et al., 2024). This paroxysmal sequence exhibited 17 lava fountain episodes that reached heights of several hundred meters along with tall columns of ash and steam rising several kilometres above the crater, together with a rapid increase of volcanic tremor (Bonaccorso et al., 2021; Calvari and Nunnari, 2022). After a quiet period of 48 days, during which occasional intracrateric Strombolian activity gradually decreased, intense eruptive activity resumed with a vigorous Strombolian episode on May 19, 2021, marking the onset of a new paroxysmal sequence that lasted until late October. However, frequent paroxysms occurred until early August, with peaks of up to two events per day. Subsequently, the frequency decreased significantly, with only three events recorded thereafter (August 29, September 21, and October 23, 2021). For this study, we defined the period between May 19 and August 14 as 'Sequence 2 (SEQ2)', considering the InSAR data that will be discussed in the following sections. By the end of February 2022, 66 paroxysmal events had been registered since the first onset in December 2020 (Calvari and Nunnari, 2022), all following a relatively similar evolutionary pattern, consistent with previous sequences at Etna such as those that occurred between 2011 and 2012 (Behncke et al., 2014; Viccaro et al., 2014). Ash and lapilli fallout from eruptive plumes represented a significant hazard to residents and infrastructure in the densely populated areas surrounding the volcano, as well as a major risk to aviation.

The characteristics and recurrence of these paroxysmal sequences, combined with the deformation signals recorded during both the pre-paroxysmal and paroxysmal periods, motivate a detailed geodetic investigation of the magmatic processes underlying the entire 2020–2022 eruptive cycle. While previous studies have investigated the 2020–2022 eruptive cycle from petrological and volcanological perspectives, characterising differences in magma composition and erupted volumes between the two sequences (Corsaro et al., 2024; Proietti et al., 2023), the geodetic dimension of this cycle and in particular the causal relationships between deep magmatic recharge, flank dynamics, and the onset and contrasting character of the two paroxysmal sequences has not been systematically addressed. This study fills this gap through an integrated geodetic investigation covering both paroxysmal sequences and the one-year pre-paroxysmal period preceding them. By combining Global Navigation Satellite System (GNSS) and Interferometric Synthetic Aperture Radar (InSAR) time series analysis with analytical deformation source modelling, we investigate the dynamics of Etna's shallow feeding system and the processes driving the observed deformation. Specifically, we examine how similar the two paroxysmal sequences are and what differentiates them, what the observed

deformation reveals about the structure of Etna's plumbing system, what characterises the recharge process over the study period, and what this eruptive cycle reveals about the causal relationships between flank dynamics and volcanic activity.

Methods

GNSS

Ground deformation at Etna volcano is monitored by the *Osservatorio Etneo* of the Italian National Institute of Geophysics and Volcanology (INGV-OE). We processed daily RINEX files from 34 permanent GNSS stations of the INGV GNSS network (Fig. 2) covering the period January 2020 to March 2022. These stations provide continuous measurements with a network distribution that covers the entire volcano, from its base up to the summit area. We computed daily position time series in static mode using NASA's Jet Propulsion Laboratory (JPL) GipsyX 2.2 software (Bertiger et al., 2020) in precise point positioning (PPP) mode (Zumberge et al., 1997), including phase ambiguity resolution. We used JPL final orbits and satellite clock products, as well as the FES2014b model (Carrére et al., 2016) for the correction of ocean tidal loading and the new gridded Vienna Mapping Function (VMF1) model (Kouba, 2008) for tropospheric corrections. The positional time series are relative to the Mount Etna Reference Frame (MERF23; Palano et al., 2023) to separate deformation linked to volcanic activity from the regional tectonic signal.

InSAR

We processed 236 SAR images acquired by the European Space Agency's (ESA) Sentinel-1 satellite (C band, wavelength ~5.6 cm) to generate small-baseline interferograms. The dataset comprises 128 ascending-track images (path 44) and 108 descending-track images (path 124), collected between January 2020 and March 2022, providing full coverage before, during, and after the paroxysmal sequences.

The InSAR processing consisted of two main steps: interferogram generation and stacking, followed by time-series analysis. Interferograms were formed using the Sentinel stack processor (Fattahi et al., 2016) within the ISCE software (Rosen et al., 2012), pairing each SAR acquisition with its five next neighbours to increase network redundancy. This produced 325 ascending and 525 descending interferograms with a maximum temporal baseline of 30 days (Fig. 3). Topographic contributions were removed using the 30-m SRTM DEM, and orbital errors were corrected using precise orbit files. We used a Goldstein low-pass filter (Goldstein and Werner, 1998) to enhance signal-to-noise ratio,

with a strength of 0.6. Interferograms were unwrapped using the SNAPHU algorithm (Chen et al., 2000) and geocoded to transform results from radar to geographic coordinates. For time series analysis, we used the SBAS-based MintPy software (Yunjun et al., 2019), removing low-coherence interferograms. Subsequently, we applied a correction for tropospheric delay based on the ERA-Interim atmospheric model to reduce the stratified component of the trospospheric delay (Doin et al., 2009), though shorter-wavelength atmospheric turbulence may persist.

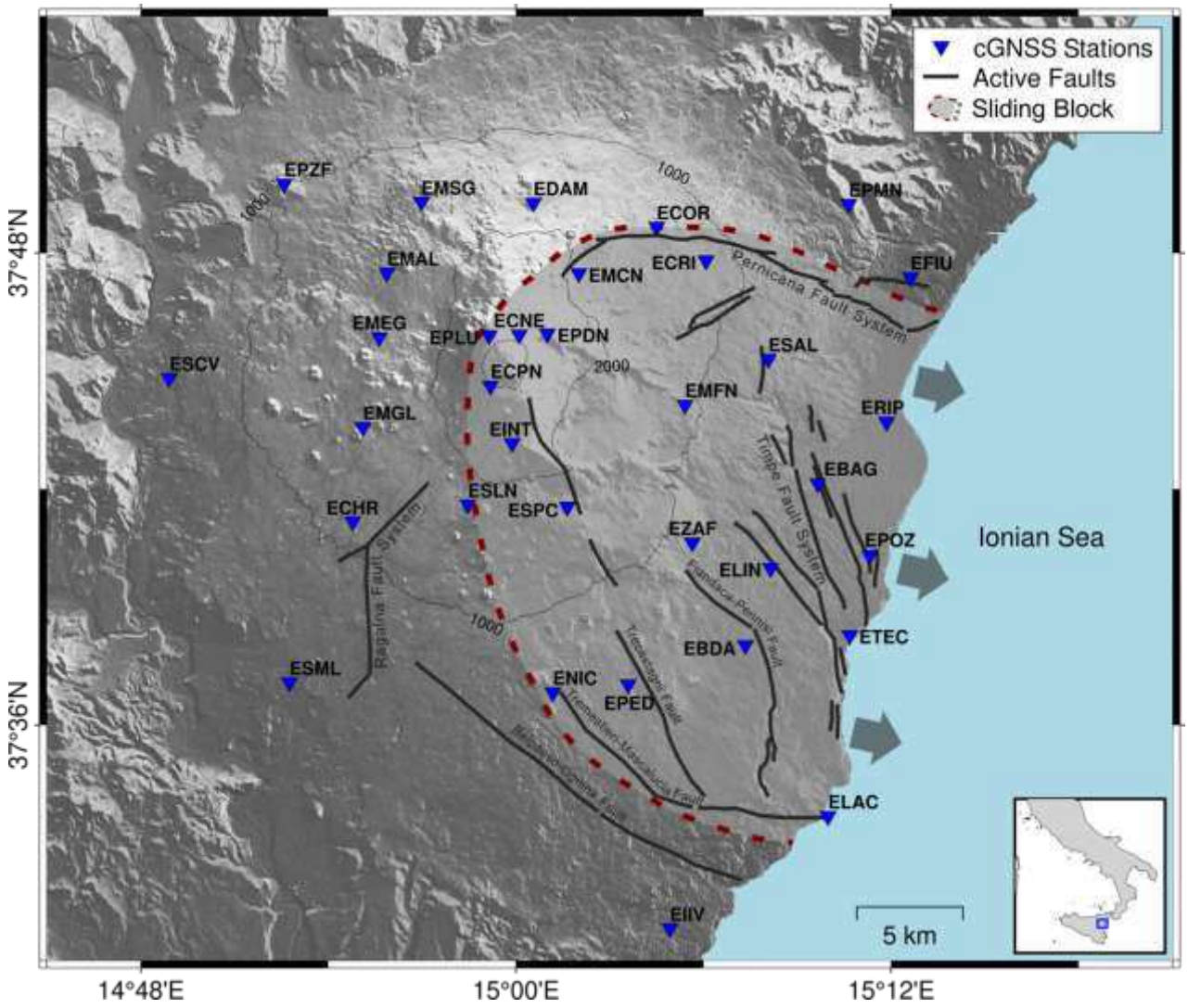


Fig. 2 Distribution of the 34 GNSS stations (blue triangles) used in this study. The map highlights the main regional fault systems, based on Bonforte et al. (2013): the Pernicana Fault System, Timpe Fault System, Ragalna Fault System, Fiandaca–Pennisi Fault, Trecastagni Fault, Tremestieri–Mascalucia Fault, and Belpasso–Ognina Fault. The dashed red line indicates the sliding sector

For deformation analysis, we focused on three periods: the one-year pre-paroxysmal period, SEQ1 (mid-February to end of March 2021), and SEQ2 (mid-May to mid-August 2021). Following Yunjun et al. (2021), we estimated Line-of-Sight (LOS) velocities and converted them to cumulative displacements assuming linear deformation. For SEQ1, cumulative displacements were computed

from images acquired on 28 January and 10 April 2021 for both ascending and descending geometries. For SEQ2, we used 16 May and 14 August 2021 for the ascending track, and 4 May and 21 July 2021 for the descending track. Interval endpoints were defined based on the decrease in deformation rates.

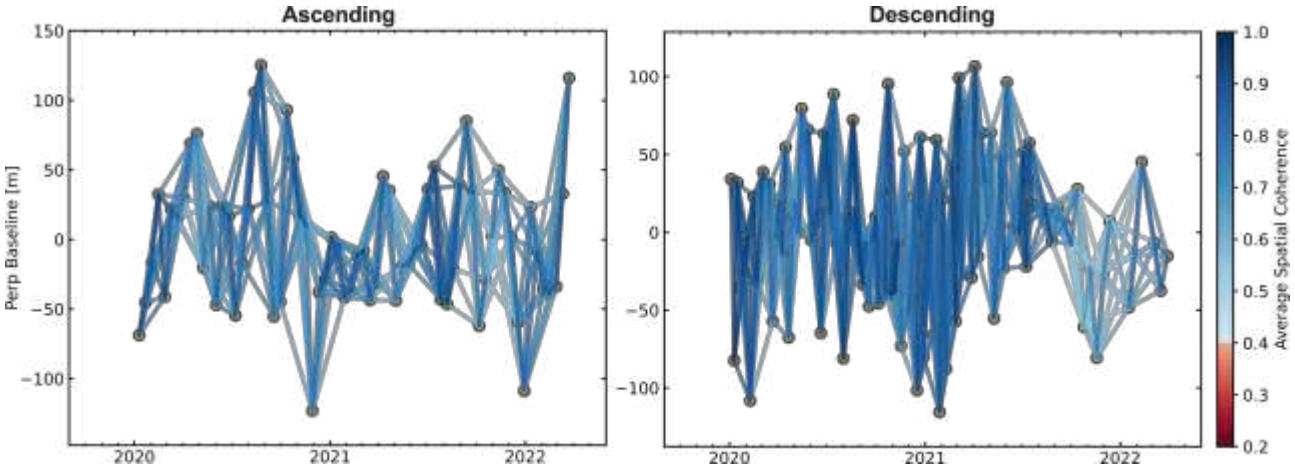


Fig. 3 Interferogram networks for ascending (left) and descending (right) views. Each node represents a SAR acquisition, and each line represents an interferogram formed between two acquisitions

The 3D SISTEM algorithm: integrating GNSS and InSAR data

GNSS provides high-accuracy three-component displacement vectors at discrete measurement points, while InSAR offers spatially continuous coverage over large areas but retrieves only the line-of-sight (LOS) component of displacement, primarily sensitive to vertical and east–west motion due to the near-polar orbits of SAR satellites (Pinel et al., 2014). To exploit the complementary strengths of both techniques, we apply the SISTEM algorithm, which combines LOS displacements with nearby GNSS observations through a weighted least-squares inversion to resolve 3D displacement components at each pixel, without interpolating GNSS values onto the InSAR grid. The influence of each GNSS station decays with distance from the target point. For further details we refer to Guglielmino et al. (2011).

In this study, we used the InSAR cumulative displacements calculated separately for each paroxysmal sequences and for the preceding period, together with GNSS measurements from the same periods. This approach ensures a linear trend of the observed deformation during each period. We referenced both GNSS and InSAR observations to the EIIV station of the INGV GNSS-network, located in the city of Catania, about 30 km from Etna's summit. Of the 34 initially processed GNSS stations, we selected the 31 that provided uninterrupted data coverage during both paroxysmal sequences.

Deformation modelling

We performed analytical modelling using idealised source geometries to constrain the location and shape of the sources responsible for the observed deformation during the two 2021 paroxysmal sequences and the preceding pre-paroxysmal period. Because the deformation field displays a semi-radial pattern centred close to the summit, we considered a prolate spheroidal source (Yang, 1988), which provides a more realistic representation of a finite pressurised body than a classical point source. The Yang model parameters include major semi-axis length, aspect ratio between the semi-axes, strike and plunge of the major axis, volume change, depth, and horizontal position of the source. We assumed a homogeneous, isotropic, elastic half-space with a Poisson's ratio of 0.25 and a shear modulus of 30×10^9 Pa. We used the MATLAB-based GAME software package (Cannavò, 2019), which employs a combination of Genetic Algorithm, Pattern Search, and Nonlinear Least Squares optimisation to ensure robust convergence of the model parameters. Parameter uncertainties were assessed using Jackknife resampling (Efron et al., 1981), recalculating the model while systematically omitting one data point at a time. Topographic corrections were applied following Williams and Wadge (1998).

Results

Temporal Evolution of Ground Deformation

The geodetic measurements reveal distinct deformation patterns associated with the paroxysmal activity, with SEQ1 showing more intense and spatially extensive deformation field, affecting the entire volcanic edifice compared to SEQ2, which produced more localised ground displacements. Prior to the paroxysmal activity, a volcano-wide displacement field had already developed during 2020, exhibiting variable deformation patterns across different sectors of the volcano. Fig. 4 presents the GNSS time series for a selection of representative stations, grouped by distance to the summit area into three categories: summit, mid-flank and peripheral stations. Figs. 5-7 show the joint InSAR and GNSS measurements, together with the 3D displacements reconstructed using the SISTEM algorithm.

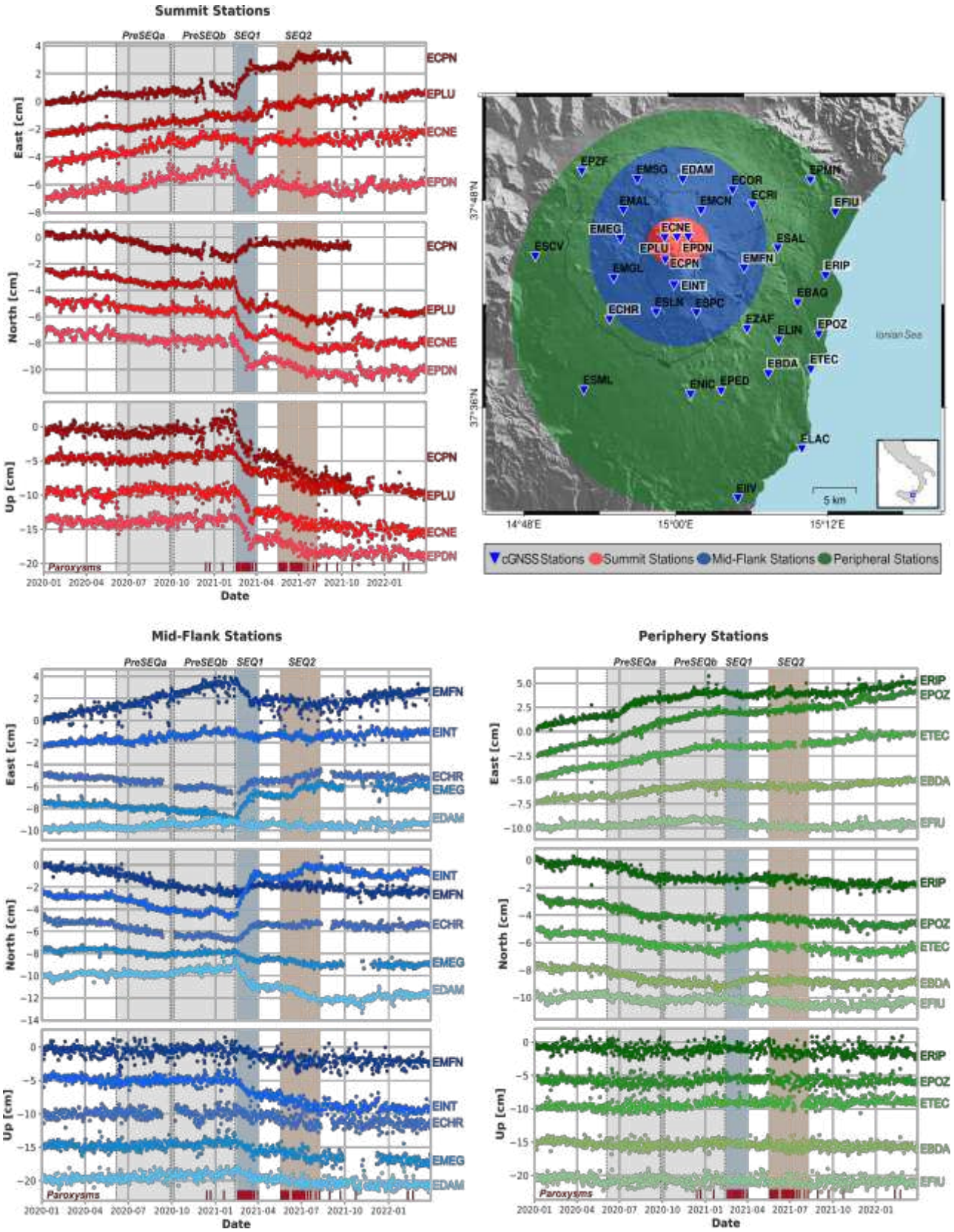


Fig. 4 GNSS time series of daily solutions from January 2020 to March 2022 for selected stations (highlighted in the map at the top right), grouped according to their distance from the summit: Summit stations (red), located within 1–2 km of the active craters (top left); Mid-flank stations (blue), situated 5–10 km from the summit (bottom left); and Peripheral stations (green), located 10–20 km from the summit on the Eastern flank (bottom right). Blue (SEQ1) and orange (SEQ2) shaded bands indicate paroxysmal sequences 1 and 2, respectively, while the grey bands, PreSEQa and PreSEQb, correspond to intervals used for modelling during the pre-paroxysmal period, with distinct ground deformation signatures. The red bars at the bottom of the plots mark the timing of individual paroxysms

Pre-Paroxysmal Deformation Patterns

Figure 5 shows horizontal GNSS displacement vectors diverging radially from the northwestern sector, dominating over the vertical component during this period. Larger vertical displacements concentrate in the northwestern sector, while the eastern flank shows a heterogeneous pattern with some stations exhibiting uplift and others subsidence. Only summit and northwestern stations show a consistent uplift pattern, with peak amplitudes of approximately 1.8 cm during the month preceding the onset of paroxysmal activity in February 2021. The InSAR-derived cumulative displacement fields and the SISTEM-derived 3D displacement maps reveal subsidence along the Pernicana and Fiandaca fault systems, with subsidence of up to 1.5 cm along these structures (Fig. 5).

The dominant deformation signal throughout this period reflects the significant eastward movement of Etna's eastern flank (Bonforte et al., 2011; Poland et al., 2017; Murray et al., 2018; Urlaub et al., 2018), with coastal stations recording displacements of up to 4.5,cm, bounded to the north by the Pernicana fault system and to the south by the Trecastagni fault, suggesting that these structures may play a role in accommodating deformation during this period.

The horizontal GNSS components (Fig. 4) allow us to distinguish two deformation phases during the pre-paroxysmal period, PreSEQa and PreSEQb, based on changes in displacement rate. PreSEQa spans from late May to the late September 2020 and PreSEQb extends from October to mid-February 2021, just before the onset of the first paroxysmal sequence SEQ1. Both phases are characterised by a slope change in the displacement time series, visible across nearly all stations, reflecting a progressive acceleration of ground motion leading up to SEQ1. Summit stations show a slope change in the horizontal components by the end of May indicating increased motion towards the south and east, consistent with a deformation source beneath the northwestern sector (Fig. 4), first identified by Nunnari and Puglisi (1994) and subsequently confirmed by multiple geodetic studies (Puglisi et al., 2001, 2004; Bonaccorso et al., 2011; Palano et al., 2024).

The eastward flank displacement signal intensifies progressively in both the GNSS and InSAR time series, with this acceleration particularly evident over the five months preceding the onset of paroxysmal activity in December 2020.

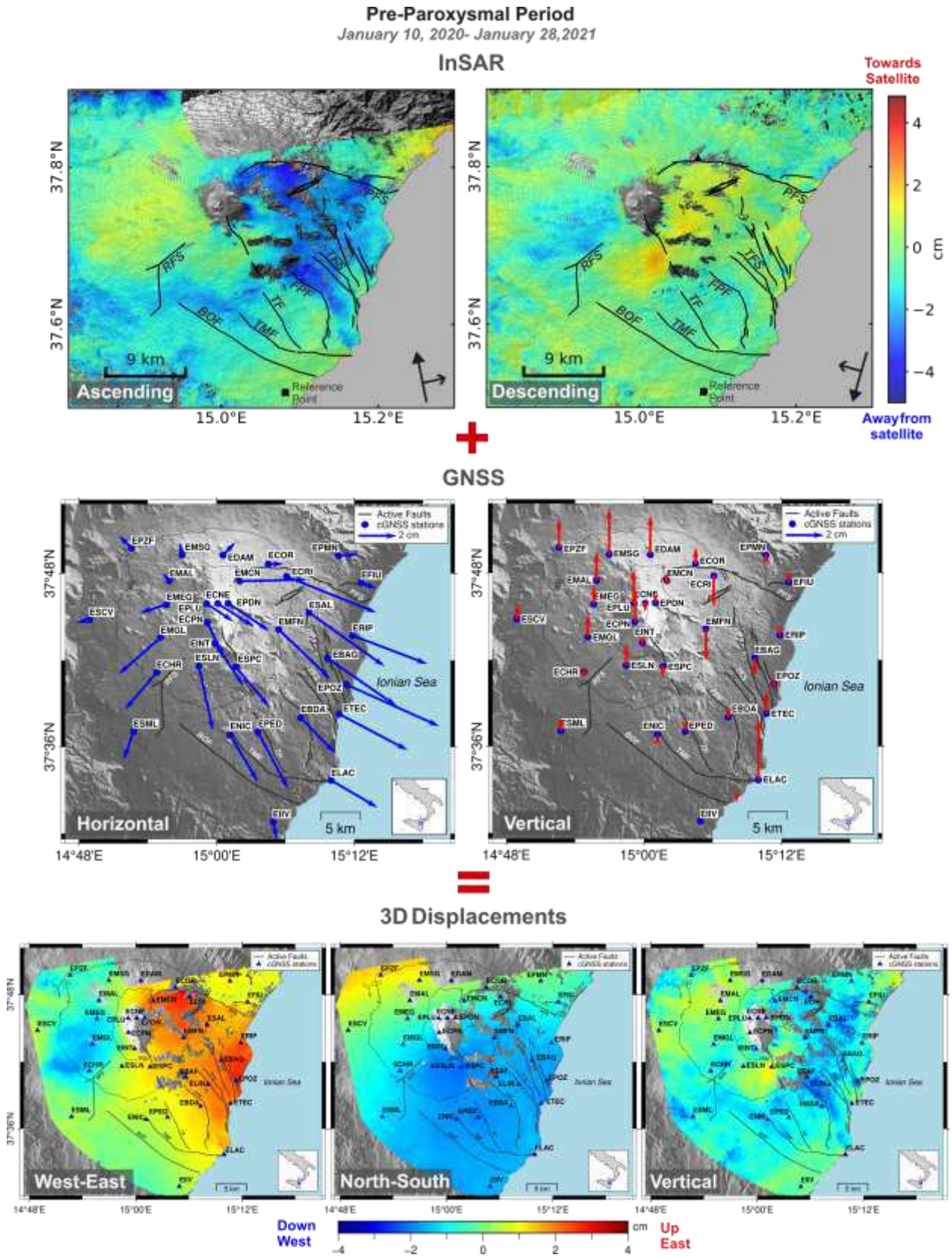


Fig. 5 Ground deformation during the pre-paroxysmal period (January 2020–January 2021). (Top) Cumulative displacement maps from ascending (left) and descending (right) InSAR acquisitions. Regions lacking interferometric coherence are left uncoloured. (Middle) Horizontal (left) and vertical (right) GNSS displacement vectors. (Bottom) Three-dimensional ground deformation field components: East (left), North (centre), and Vertical (right), derived using the SISTEM algorithm through the integration of InSAR and GNSS data. The maps include the main regional fault systems: (PFS) the Pernicana Fault System, (TFS) Timpe Fault System, (RFS) Ragalna Fault System, (FPF) Fiandaca–Pennisi Fault, (TF) Trecastagni Fault, (TMF) Tremestieri–Mascalucia Fault, and (BOF) Belpasso–Ognina Fault

Co-Paroxysmal Deformation Patterns – Sequence 1 (SEQ1)

Figure 6 shows an intense deflation trend across the entire volcanic edifice between mid-February and early April 2021. Horizontal displacement vectors from the GNSS network, including stations located on the eastern flank and near the coast up to 20 km from the summit, consistently show a centripetal pattern towards the summit. This behaviour indicates that the entire volcanic edifice was affected by the magmatic activity of this paroxysmal sequence. The typical eastward motion of the eastern flank (Bonforte et al., 2011) appears to be masked during this interval by the dominant centripetal signal. In contrast, the western flank exhibited larger horizontal displacement magnitudes, as revealed by the InSAR data. The 3D displacement field obtained by combining GNSS and InSAR datasets reveals an intense deflation in the summit area of about 4.5 cm in the vertical component and maximum values reaching 3.8 cm in the horizontal components (Fig. 4).

Moreover, the GNSS displacement vectors reveal a systematic decrease in magnitude with distance from the summit: mid-flank stations recorded horizontal displacements of up to 2 cm, while those located on the lower slope zones reached maximum displacements of approximately 1 cm in horizontal components. This response suggests that the observed displacement corresponds to a coherent, edifice-wide deformation field excluding any hypotheses of local effects driven by structural features of the volcano.

Co-Paroxysmal Deformation Patterns – Sequence 2 (SEQ2)

Figure 7 shows the ground deformation for SEQ2. In contrast to SEQ1, where volcano-wide deflation affected even distal coastal stations, the deformation field during SEQ2 is more spatially confined, with clear attenuation of the displacement signal at coastal GNSS stations. The strongest deformation remains concentrated in the summit area. Summit sector stations recorded vertical displacements of approximately -1.5 cm and horizontal variations of approximately 1 cm during the 18-day sub-period. From 8 July onward, a flattening trend in the GNSS displacement time series reflects the decreasing frequency of paroxysmal events.

The analysis of SEQ2 is limited to events up to 14 August 2021, constrained by the temporal coverage of available InSAR acquisitions, during which a coherent deformation signature was identifiable across the volcano. Three additional paroxysms occurred on 29 August, 21 September, and 23 October 2021, separated by intervals of several weeks. Geodetic observations covering these events did not capture coherent volcano-wide deformation patterns comparable to those observed during the main sequence. These paroxysms are therefore excluded from the deformation analysis.

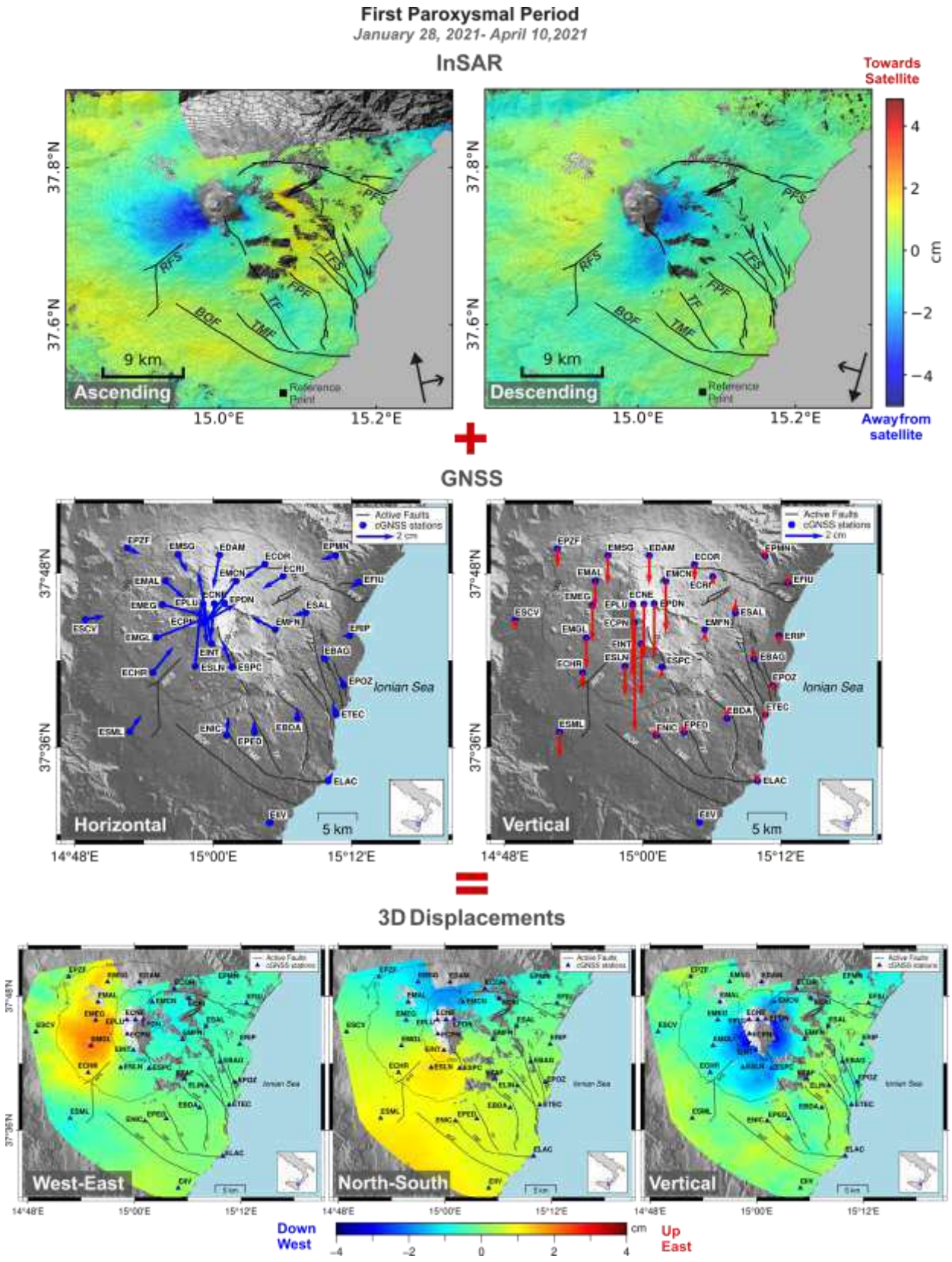


Fig. 6 Ground deformation during the paroxysmal Sequence 1 (February 2021 - April 2021). (Top) Cumulative displacement maps from ascending (left) and descending (right) InSAR acquisitions. Regions lacking interferometric coherence are left uncoloured. (Middle) Horizontal (left) and vertical (right) GNSS displacement vectors. (Bottom) Three-dimensional ground deformation field components: East (left), North (centre), and Vertical (right), derived using the SISTEM algorithm through the integration of InSAR and GNSS data. The maps include the main regional fault systems: (PFS) the Pernicana Fault System, (TFS) Timpe Fault System, (RFS) Ragalna Fault System, (FPF) Fiandaca–Pennisi Fault, (TF) Trecastagni Fault, (TMF) Tremestieri–Mascalucia Fault, and (BOF) Belpasso–Ognina Fault

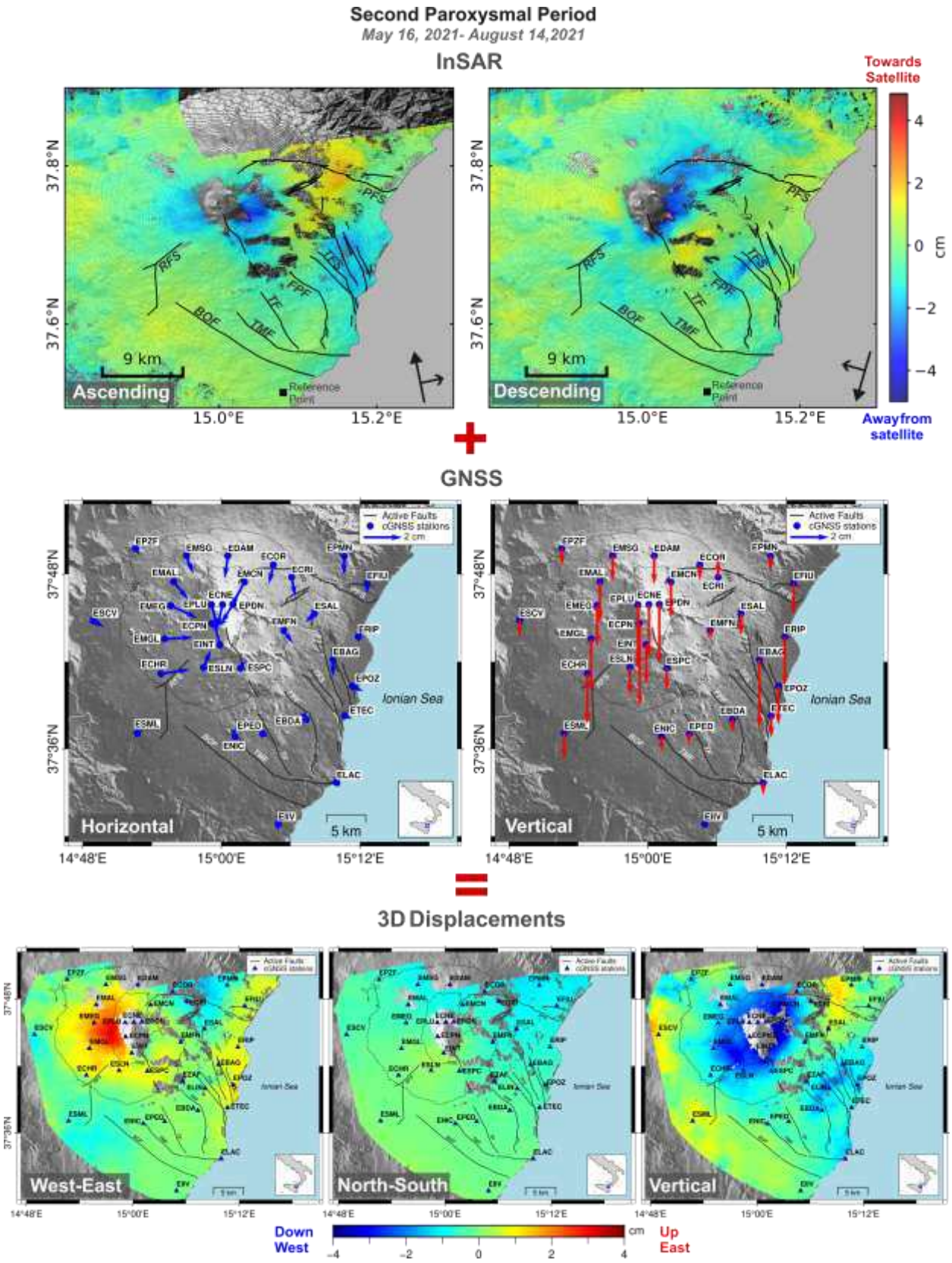


Fig. 7 Ground deformation during the paroxysmal Sequence 2 (May 2021 - August 2021). (Top) Cumulative displacement maps from ascending (left) and descending (right) InSAR acquisitions. Regions lacking interferometric coherence are left uncoloured. (Middle) Horizontal (left) and vertical (right) GNSS displacement vectors. (Bottom) Three-dimensional ground deformation field components: East (left), North (centre), and Vertical (right), derived using the SISTEM algorithm through the integration of InSAR and GNSS data. The maps include the main regional fault systems: (PFS) the Pernicana Fault System, (TFS) Timpe Fault System, (RFS) Ragalna Fault System, (FPF) Fiandaca–Pennisi Fault, (TF) Trecastagni Fault, (TMF) Tremestieri–Mascalucia Fault, and (BOF) Belpasso–Ognina Fault

Figure 8 shows the 3D displacement fields derived from the SISTEM algorithm for the three analysed periods. During the pre-paroxysmal period, horizontal displacement vectors radiate from the northwestern sector and increase in magnitude with distance from the summit. Despite differences in displacement magnitude, both paroxysmal sequences show broadly similar deformation patterns, including large horizontal displacements on the western flank and pronounced subsidence focused around the summit area.

The two sequences differ in their spatial distribution. SEQ1 displays a relatively homogeneous and widespread deflation across the volcanic edifice. SEQ2 reveals distinct deformation sectors: displacement vectors on the eastern flank show seaward motion, while vectors on the southern and western flanks display a different orientation, suggesting the involvement of additional deformation sources beyond those active during SEQ1.

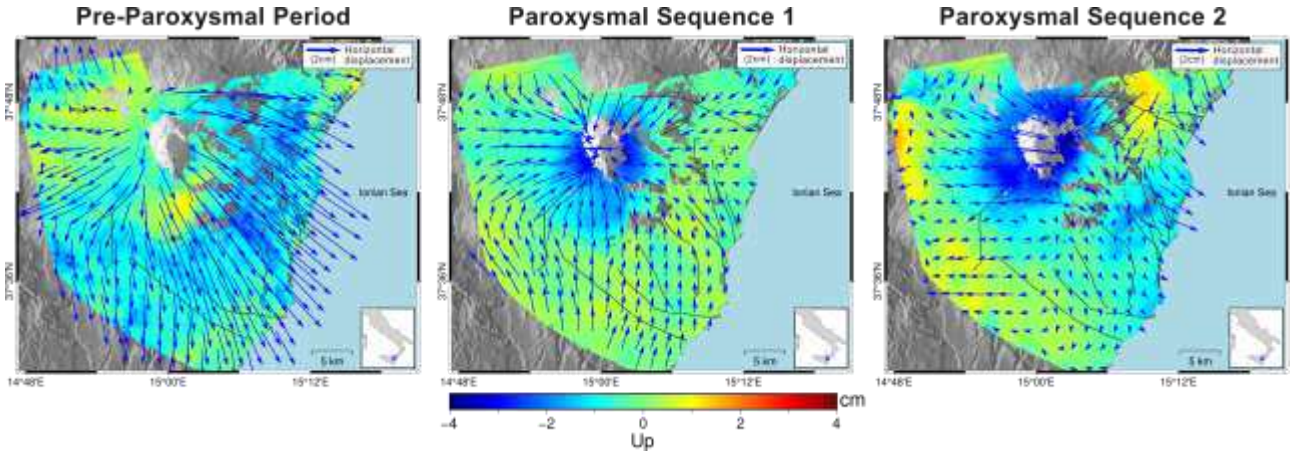


Fig. 8 Three-dimensional displacement maps derived using the SISTEM algorithm for the pre-paroxysmal period (left), Sequence 1 (middle), and Sequence 2 (right). Horizontal displacements are shown by blue vectors, and the vertical component is represented by the color scale. The main fault systems are outlined in black

Modelling results

We performed separate geodetic inversions (10^6 iterations each) using the GNSS-only and integrated SISTEM datasets. As InSAR data decorrelated during the pre-paroxysmal period, resulting in unreliable interferograms, it was not possible to subdivide this interval into the two phases identified from the GNSS time series and volcanic activity records from other sources (such as seismic and volcanic gas observations). We therefore used the GNSS-only dataset to model the pressurised deformation sources active during PreSEQa and PreSEQb, and the SISTEM dataset to invert the observed cumulative flank motion during the pre-paroxysmal period and to model deformation sources of the paroxysmal sequences (SEQ1 and SEQ2), where InSAR data maintained high coherence. For SEQ2, we excluded the final three paroxysms of 2021 (August 29, September 21, October 23), as they showed no significant ground displacement, suggesting limited or reduced

coupling with the shallow reservoir system. All inversions assume a linear deformation trend for each modelled period. The inversion results for the four deformation periods are summarised in Table 2 and illustrated in Figs. 9–12.

Pre-paroxysmal period: we subdivided the pre-paroxysmal period into two phases based on changes in GNSS displacement rates (Fig. 4) and volcanic activity documented in INGV-OE bulletins, including increased tremor amplitude and elevated surface CO_2 flux from 21 May 2020 onwards (INGV-OE, 2020). We first inverted the SISTEM dataset for the full pre-paroxysmal period to characterise the flank-related deformation of the Eastern sector, the most prominent and coherent feature visible throughout this period (Fig. 5). To model this cumulative signal, we adopted an Okada-type dislocation (Okada, 1985) representing a sliding plane, consistent with previous studies of Etna's flank dynamics (Bonforte and Puglisi, 2003; Bonaccorso et al., 2006). In this inversion, all geometric and positional parameters were treated as free variables to explore the kinematics of the eastern flank, except for the azimuth, which was fixed at 8° N to align the source with the Pernicana Fault (Bonaccorso et al., 2006), as summarised in Table 1. The inversion yields a dislocation plane dipping 11.7° at ~1.5 km b.s.l., consistent with earlier results (Bonaccorso et al., 2006; Bonforte and Puglisi, 2006; Puglisi et al., 2008). We then used this Okada geometry as a fixed component in the phase-specific inversions.

For each pre-paroxysmal phase (PreSEQa, PreSEQb), we performed joint inversions of a pressurised Yang-type source together with the fixed Okada dislocation. Because GNSS-only data could not uniquely resolve the ellipsoidal geometry of a Yang source, we fixed its aspect ratio at 0.5 to minimise depth-geometry trade-offs. For the first phase (late May to late October 2020), the inversion identifies a Yang-type source located approximately 5.5 km below sea level, producing a volume increase of $(7.3 \pm 0.38) \times 10^6$ m³. During the second phase (late October 2020 to mid-February 2021), the source migrated upward to 4.2 km below sea level and produced a smaller volume increase of $(5.9 \pm 0.24) \times 10^6$ m³.

Paroxysmal Sequences: we inverted the SISTEM-derived displacement fields for both paroxysmal sequences using a deflating Yang-type source. We also tested joint inversions combining a Yang source with the Okada dislocation for the flank motion and evaluated the model performance using the Akaike Information Criterion (AIC; Akaike, 1974), which quantifies the trade-off between model complexity and goodness of fit, favouring models that achieve sufficient explanatory power with the fewest parameters. According to the AIC results (Table 3), the displacement field of SEQ1 is satisfactorily reproduced by the Yang source alone, whereas the inclusion of the Okada dislocation significantly improves the fit for Sequence 2, indicating the contribution of fault-related motion and

stress accommodation along the eastern flank during this interval. The inferred volume changes are relatively similar between the two events, with values of (−7.3 ± 0.12) × 10^6 m^3 during Sequence 1 and (−7.2 ± 0.43) × 10^6 m^3 during Sequence 2. However, the source migrated upward by ~843 m between sequences, from 3,760 ± 73 m below sea level (Sequence 1) to 2,917 ± 540 m below sea level (Sequence 2).

Parameter uncertainties increase substantially from Sequence 1 to Sequence 2, suggesting that the deformation field became more complex during the second sequence and was likely influenced by the superposition of several magmatic processes rather than by a single dominant source (see Discussion).

Table 1 Model parameters for the Okada source derived from the SISTEM inversion of the pre-paroxysmal period

Parameter	PreSEQ	PreSEQa	PreSEQb	SEQ1	SEQ2
East[a] [m]	505 671 ± 62	505 671	505 671	505 671	505 671
North[a] [m]	4 171 753 ± 20	4 171 753	4 171 753	4 171 753	4 171 753
Depth [m b.s.l.]	-1511 ± 40	-1511	-1511	-1511	-1511
Azimut[b]	8	8	8	8	8
DIP	11.7 ± 0.2	11.7	11.7	11.7	11.7
Length	28 901 ± 38	28 901	28 901	28 901	28 901
Width	35 000 ± 35.3	35 000	35 000	35 000	35 000
Stk-slip	-0.018 ± 8e-5	-0.012 ± 0.0001	-0.002 ± 2e-05	-0.002 ± 0.0004	-0.002 ± 0.0009
Dip-slip	0.035 ± 0.0003	0.018 ± 0.0001	0.007 ± 0.0001	0.001 ± 0.001	0.01 ± 0.003
Tensil	-0.003 ± 0.0002	0.005 ± 0.0001	0.006 ± 0.0001	0.001 ± 8e-5	-0.002 ± 0.0005

Pre-SEQ(a): 20200520-20201001; **Pre-SEQ(b)**: 20201001-20210215: **SEQ1:** 20210215 – 20210401; **SEQ2:** 20210518-20210801;

[a] Easting and Northing coordinates are given in the UTM 33N projection and refer to the position of the top centre of the plane.

[b] Azimuth fixed at 8° N to align the source with the Pernicana Fault.

Table 2 Model parameters obtained from GNSS inversions for PreSEQ(a) and PreSEQ(b), and from SISTEM inversions for SEQ1 and SEQ2

Parameter	PreSEQ(a)	PreSEQ(b)	SEQ1	SEQ2
East[a] [m]	497 184 ± 66	500 050 ± 87	499 922 ± 105	500 664 ± 433
North[a] [m]	4 181 571 ± 170	4 180 900 ± 66	4 177 035 ± 160	4 178 251 ± 195
Depth [m b.s.l.]	-5546 ± 241	-4 266 ± 171	-3 760 ± 73	-2 917 ± 540
ΔV [10^6 m^3]	7 314 723 ± 378 838	5 934 930 ± 237 487	-7 370 593 ± 121 171	-7 209 945 ± 432 001
A [m]	500 ± 299	500 ± 369	500 ± 89	500 ± 1960
b/a[b]	0.5	0.5	0.4 ± 0.12	0.2 ± 0.4
Strike [°]	201 ± 2	292 ± 2	55 ± 31	66 ± 294
Plung [°]	67 ± 1	75 ± 1	38 ± 3	41 ± 13

PreSEQ(a): 20200520-20201001; **PreSEQ(b)**: 20201001-20210215: **SEQ1:** 20210215 – 20210401; **SEQ2:** 20210518-20210801

[a] Easting and Northing coordinates are given in the UTM 33N projection and refer to the position of the top centre of the plane.

[b] Aspect ratio (b/a) fixed at 0.5 for PreSEQa and PreSEQb to minimise depth-geometry trade-offs.

Table 3 Akaike criterion (AIC) values for the different modeling configuration for each modeled period SEQ1 and SEQ2. Higher AIC values indicate a worse fit, while lower values indicate a better fit. The best-fitting model for each sequence is highlighted in bold

AIC	SEQ1	SEQ2
Yang	**1891.1**	2083.0
Yang + Okada	1896.4	**2045.8**

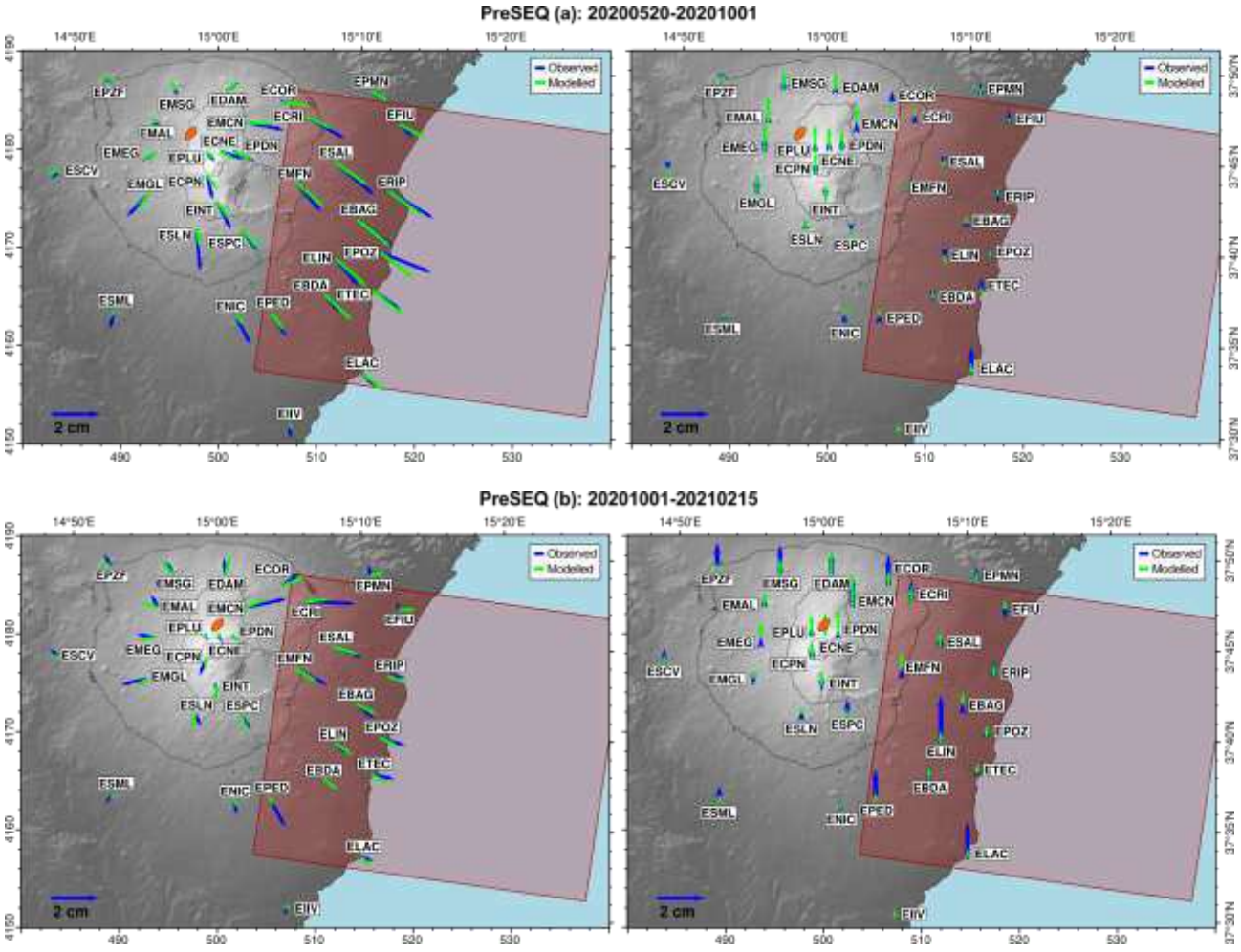


Fig. 9 Maps of measured (blue arrows) and modelled (green arrows) GNSS displacement vectors for the horizontal (left) and vertical (right) components during the pre-paroxysmal phases PreSEQa (top) and PreSEQb (bottom). The red polygon indicates the location and geometry of the Okada dislocation plane used as a fixed component in the inversion

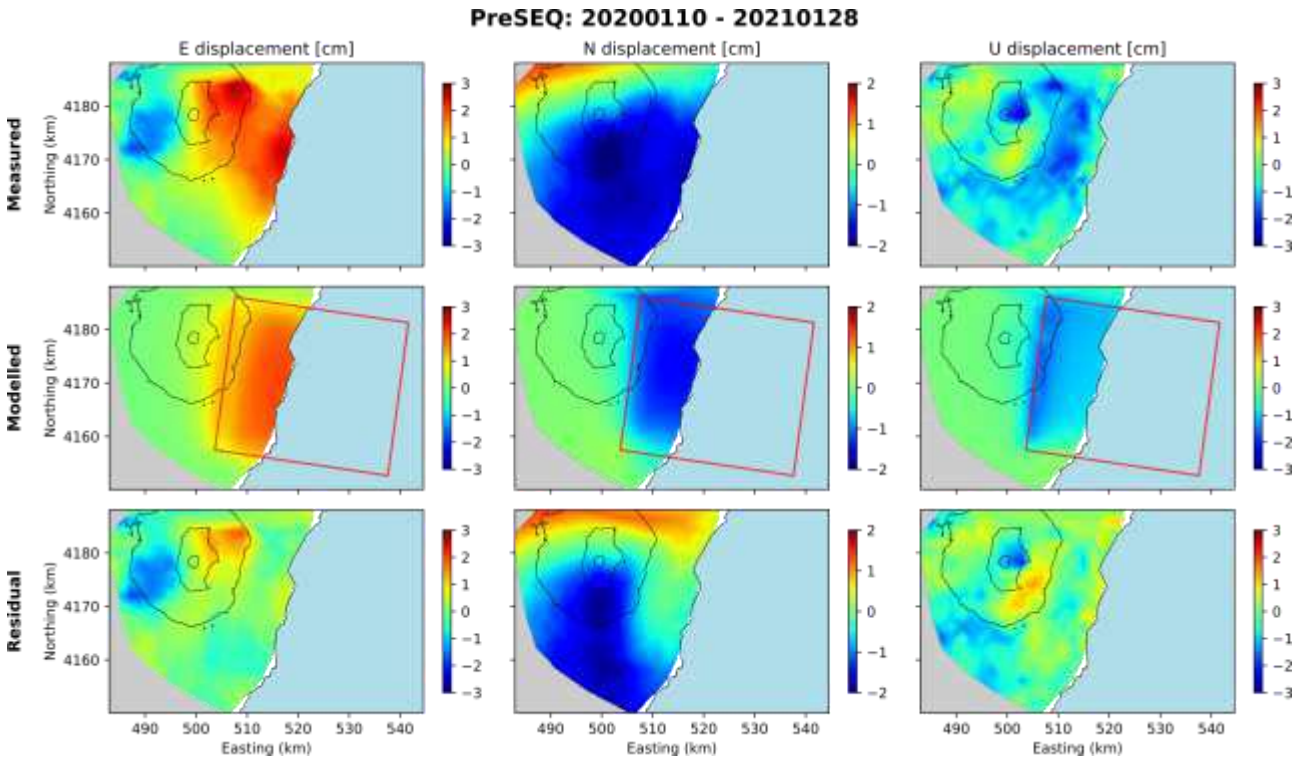


Fig. 10 Observed, modelled, and residual displacement fields for SEQ1 obtained from the inversion of the SISTEM dataset using an Okada-type dislocation

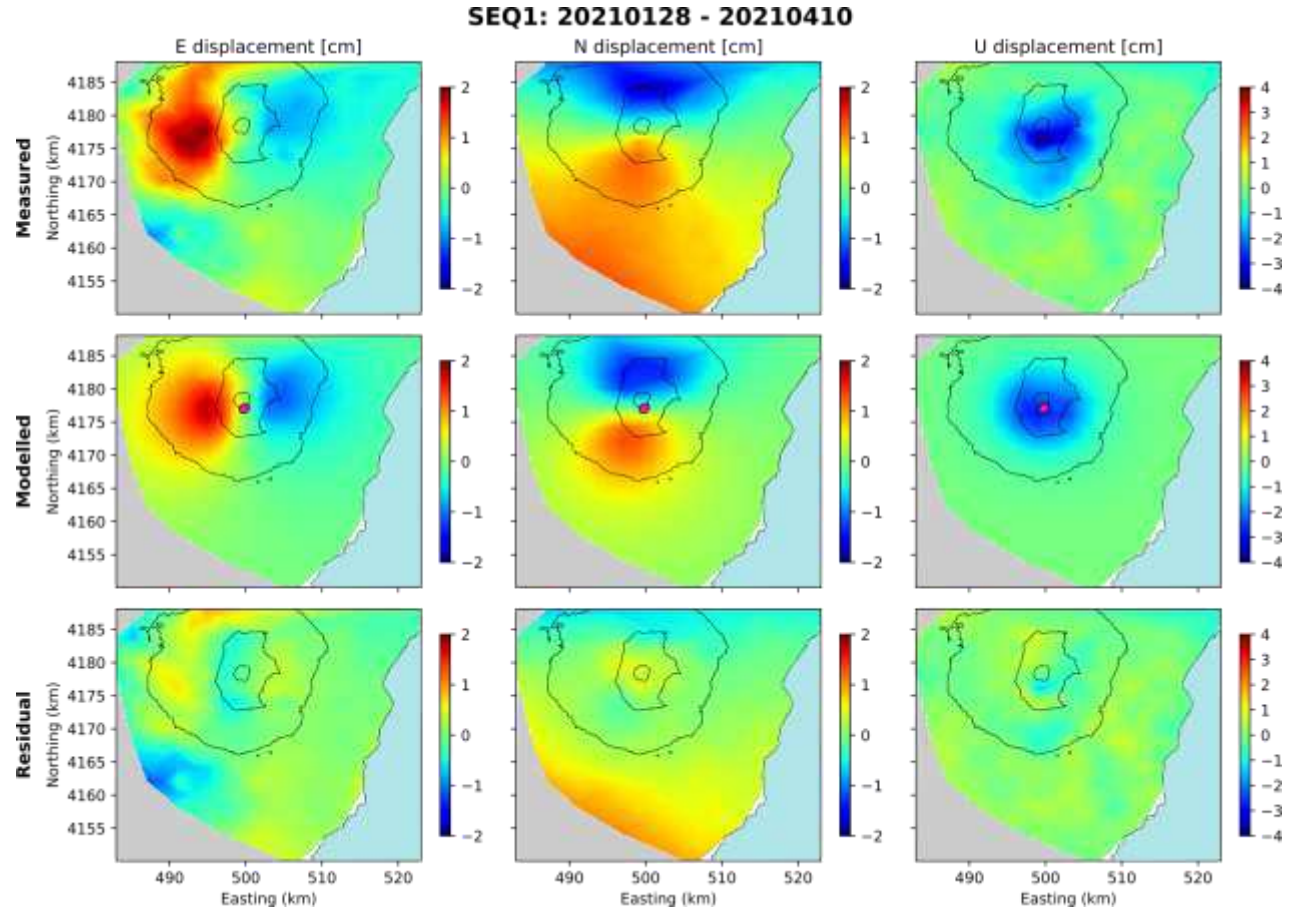


Fig. 11 Observed, modelled, and residual displacement fields for SEQ1 obtained from the inversion of the SISTEM dataset using a single Yang-type source

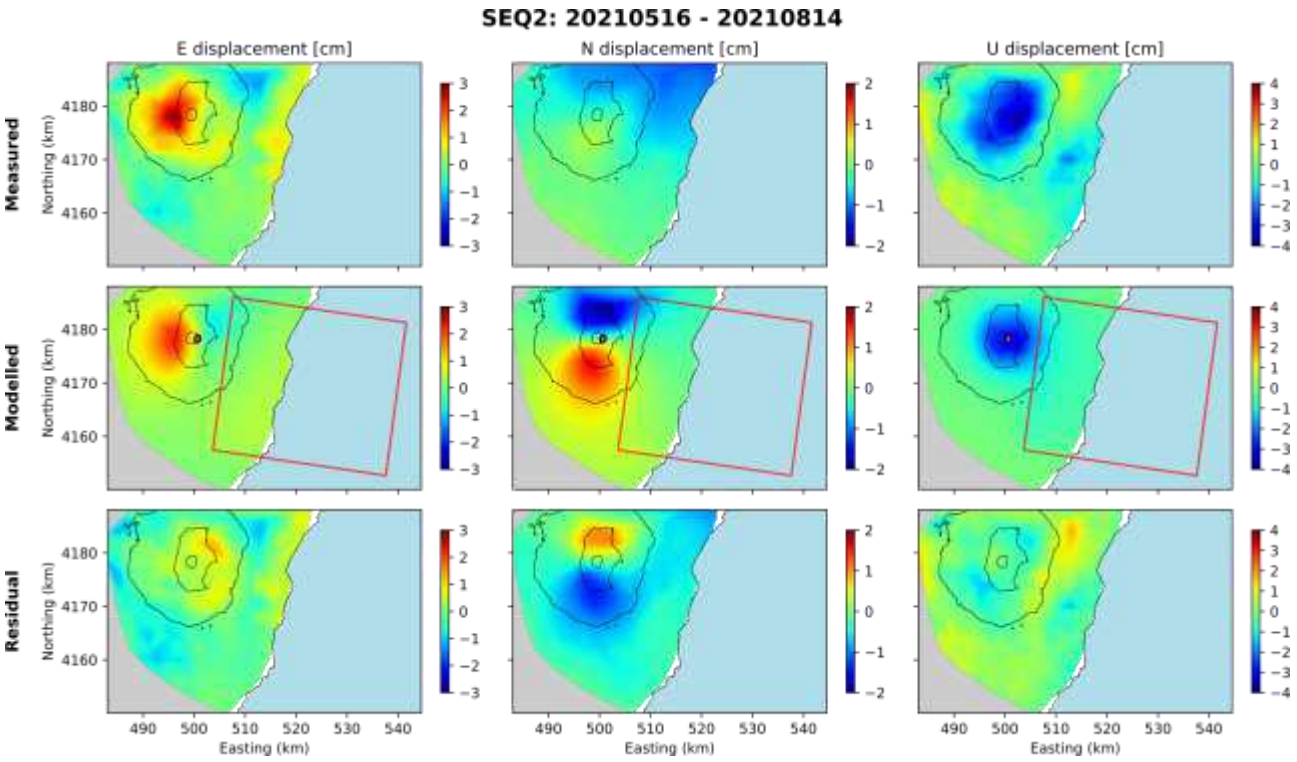


Fig. 12 Observed, modelled, and residual displacement fields for SEQ2 obtained from the inversion of the SISTEM dataset using a Yang-type source combined with an Okada dislocation

Discussion

Pre-paroxysmal deformation and progressive source migration

Geodetic observations show that ground deformation at Mount Etna, related to the eruptive activity between December 2020 and October 2021, began months before the onset of the first paroxysms at the end of 2020. The pre-paroxysmal period, defined in this study between January 2020 and February 2021, is characterised by a composite deformation field dominated by the persistent eastward motion of the eastern flank, which is one of Etna's main characteristic deformation signatures (Puglisi et al., 2004a; Bonaccorso et al., 2006; Alparone et al., 2013; Palano et al., 2023), accompanied by a less pronounced westward displacement of the western flank. This outward movement suggests lateral expansion of the volcanic edifice and is consistent with stress transfer from deep magmatic pressurisation pushing the flanks apart, rather than with shallow inflation, which produce a more symmetric and vertically dominated signal. Horizontal displacements strongly exceeded vertical motions during this interval, indicating that the observed deformation field was primarily controlled by lateral stress propagation from deep magmatic pressurisation, which has been shown to induce pronounced deformation (Acocella et al., 2016; Murray, 2019).

Source modelling reveals an upward migration of pressurised sources from approximately 5.5 km b.s.l. during PreSEQa, with a volume increase of $(7.3 \pm 0.4) \times 10^6$ m³, to approximately 4.2 km b.s.l.

during PreSEQb, with a volume increase of (5.9 ± 0.2) × 10^6 m^3. This progressive shallowing is consistent with stepwise magma transfer from an intermediate storage region toward the upper levels of the plumbing system and coincides with the transition between the two pre-paroxysmal phases identified from GNSS displacement rate changes. The inferred source depths are consistent with the deep main reservoir identified by seismic tomography at 3–9 km b.s.l. (De Gori et al., 2021) and with source depths reported in previous geodetic studies of pre-paroxysmal inflation at Mount Etna (Bonaccorso et al., 2006; Aloisi et al., 2018; Palano et al., 2017; Bonaccorso and Aloisi, 2021). The decreasing volume change between phases may reflect the progressive transfer of magma to shallower levels, contributing to the pressurisation that ultimately triggered paroxysmal activity in February 2021.

Magma-induced basement weakening and the onset of flank acceleration

The observed acceleration of the eastern flank during mid-2020 and the subsequent paroxysmal activity provide insights into the dynamics of Etna's volcanic system. Previous studies have proposed two main mechanisms to explain the behaviour of the eastern flank: gravitational spreading and magma-induced stress transfer (Borgia et al., 1992, 2000a; Lundgren et al., 2004; Neri et al., 2009; Bonaccorso et al., 2006, 2013; Murray et al., 2018). However, gravitational spreading alone cannot account for the mid-2020 acceleration, as neither significant vertical deformation nor slope-angle changes were observed during this interval, which would be expected if gravitational collapse were the dominant process. Instead, the integrated evidence presented in Fig. 13 suggests that magma-induced stress transfer was the primary driver of the observed deformation. This figure shows the temporal evolution of three different datasets: (1) GNSS displacements recorded at the EINT station, one of the most sensitive stations to detect dynamics within the shallow plumbing system, located on the southern flank near the summit; (2) depth distribution of earthquakes ranging from M0.6 to M3.7 (Barberi et al., 2022; Ferrari et al., 2024), and (3) CaO/Al2O3 ratios from glass compositions from erupted products analysed by Corsaro et al. (2024), which offer insights about the melt, indicating the primitive or evolved nature of the magma.

Within the pre-paroxysmal period, CaO/Al2O3 ratios remained at a relatively primitive baseline of approximately 0.54 through April–May 2020 (Corsaro et al., 2024), representing the resident magma composition prior to any arrival of new magma (Fig. 13, Panel 3). A change in the slope of the GNSS displacement components at the end of May, visible simultaneously across summit, mid-flank, and peripheral stations (Fig. 4), represents the earliest detectable signal of what would develop into a sustained recharge episode, preceding the first cluster of deep seismicity at 15–30 km b.s.l. in June–July 2020 by several weeks (Fig. 13, Panel 2). From late August to November 2020, approximately

2–3 months after the initial geodetic anomaly, CaO/Al2O3 ratios shift towards more evolved compositions (0.52), consistent with erupted products sourcing from a more differentiated melt relative to the April–May baseline. The subsequent shift toward more primitive compositions, peaking at 0.55–0.56 in January–early February 2021, records the physical arrival of undifferentiated recharge melt into the shallow plumbing system, an event that occurred several months after the geodetic network had captured the onset of deep intrusion.

This temporal sequence of geodetic rate change, deep seismic response and geochemical signature suggests that the GNSS network captured the onset of deep magmatic intrusion through the surface expression of stress perturbations propagating through the crust, before the ascending magma generated detectable seismicity or influenced the composition of erupted products. The correlation between geodetic acceleration, deep seismicity, and geochemical change toward evolved values, and a subsequent shift toward compositions more primitive than the pre-recharge baseline is more plausibly explained by a process such as magmatic intrusion than by gravitational expansion, which would generate neither the deep seismic signature nor the observed geochemical response. This interpretation is further supported by analogue modelling demonstrating that magmatic intrusion can act as a primary driver of flank instability even when the intrusion geometry is symmetric (Acocella et al., 2013).

The flank acceleration is consistent with stress transfer into the mechanically weak sedimentary basement underlying Etna. Previous studies have identified a deformation zone at approximately 4–5 km depth beneath the eastern flank (Apuani et al., 2013), where plastic behaviour develops under elevated temperatures and laboratory experiments demonstrate that hot, fluid-rich conditions substantially reduce rock strength and frictional resistance (Heap et al., 2013; Heap and Violay, 2021). Rising magma likely introduced heat and volatiles into this basement layer, lowering its effective yield strength and promoting lateral motion of the eastern flank.

Taken together, the network-wide geodetic precursor signal preceding seismicity by weeks and petrological response by months establishes magmatic intrusion as the initial process in the causal chain linking deep recharge, flank destabilisation, and the onset of paroxysmal activity at Mount Etna during the 2020–2022 eruptive cycle.

Seismicity and petrological signatures of deep magma recharge

Deep seismicity during the pre-paroxysmal period reveals a progressive upward migration of magmatic recharge. While seismicity concentrated predominantly within the first 10 km b.s.l., a dense cluster at 20–30 km b.s.l. emerged in late June 2020, followed by a significant increase in shallow

seismicity beneath the summit sector in August 2020, likely associated with fracturing driven by magmatic pressurisation (Scarfi et al., 2025). A new deep cluster at similar depths was recorded in October 2020, and in early December seismic activity intensified with three intermediate-depth swarms, the third occurring on 9–12 December and closely preceding the first lava fountain on 13 December. Two additional lava fountains on 21 and 22 December were similarly preceded by shallow seismicity (Bonaccorso et al., 2021). In January 2021, further deep clusters were recorded at 10–22 km b.s.l., confirming the upward migration of seismic activity. Across all three recharge pulses, seismicity migrated from depths larger than 20 km b.s.l. to 10–20 km b.s.l. and consistently concentrated in the northwestern sector of the volcanic edifice, suggesting a localised ascending magma pathway beneath this sector, an interpretation supported by the Yang source inferred from geodetic modelling (Table 2 and Fig. 9) and by the horizontal displacement vectors diverging from the same sector (Fig. 5). Deep seismicity beneath this sector has been previously interpreted as an indicator of ongoing magma movement and recharge (Alparone et al., 2012; Patanè et al., 2013; De Gori et al., 2021; Scarfì et al., 2023; Firetto Carlino et al., 2025).

The onset of intense paroxysmal activity on 16 February 2021 coincides with a significant drop in shallow seismicity within the uppermost 5 km b.s.l., reflecting a temporary reduction of stress in the shallowest crustal region. Once SEQ1 concluded, shallow seismicity rapidly resumed, revealing the persistence of magmatic unrest. During the inter-paroxysmal period, repeated earthquake clusters at 5–22 km b.s.l. indicate continued mid-crustal activity in the absence of surface eruptive activity. A further decrease in shallow seismicity marked the onset of SEQ2, consistent with renewed pressure release in the shallow system.

According to the petrological evidence of magma compositional changes throughout the pre-paroxysmal period, Corsaro et al. (2024; Fig. 13, Panel 3) found that erupted products between August 2020 and January 2021 show a trend towards more primitive compositions, with CaO/Al_2O_3 ratios increasing from 0.52 to 0.56 (R. Corsaro, pers. comm., June 2025). This shift suggests the progressive involvement of deeper magmatic sources from the pre-paroxysmal period to the onset of the first paroxysmal sequence, SEQ1. Erupted products are more primitive during the initial stages of this sequence and progressively more evolved toward its end. After a 48-day pause between the two paroxysmal sequences, eruptive activity resumed with more evolved products, followed by a renewed shift to primitive compositions as SEQ2 continued (for more details on the petrological analysis, see Corsaro et al. 2024).

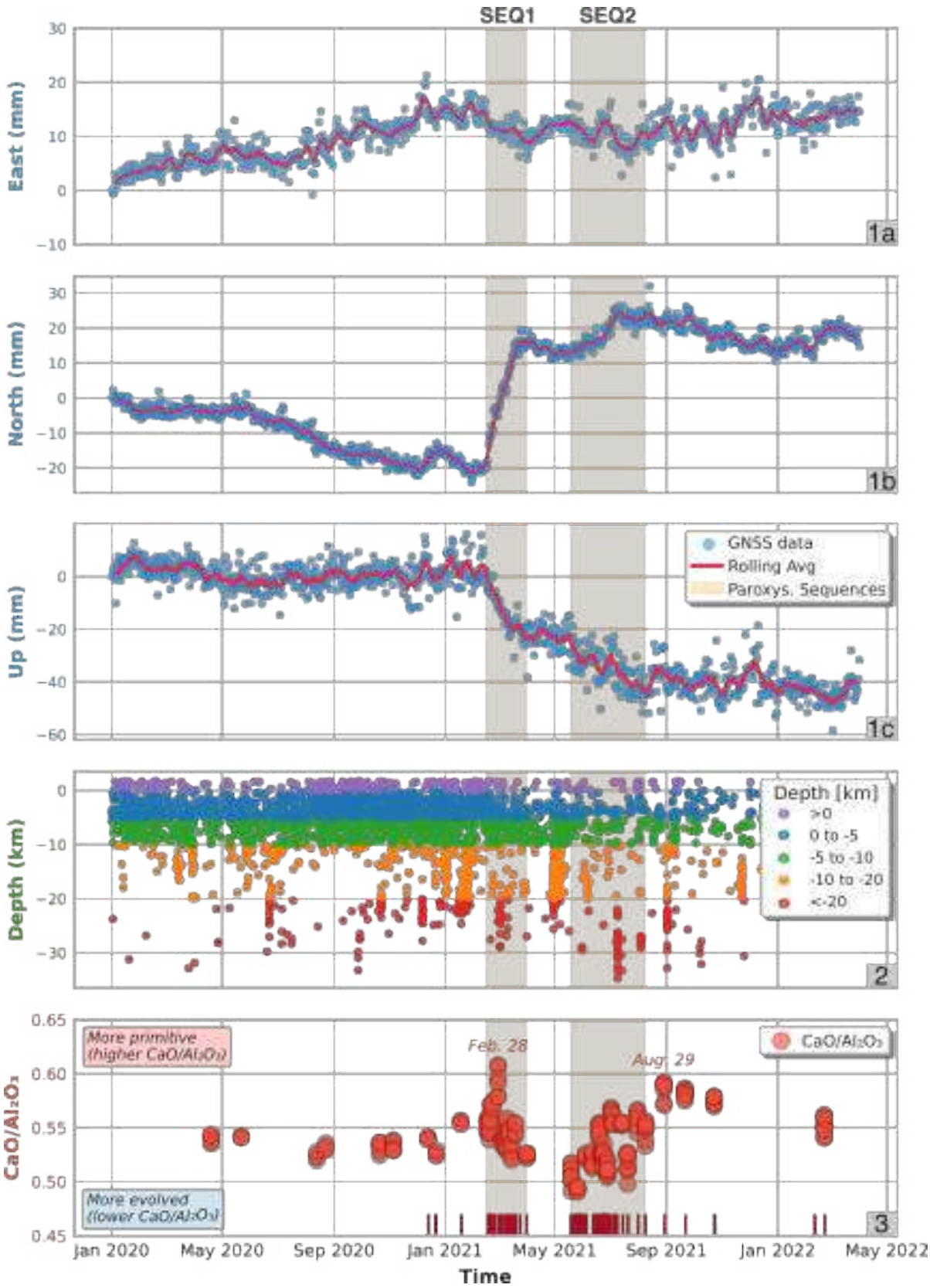


Fig. 13 Combined time series of GNSS displacement, seismicity depth, and petrological parameters from January 2020 to March 2022. (1a-1c) GNSS data represent horizontal and vertical displacements at the somital station EINT. (2) Temporal distribution of earthquake depths, categorized into five distinct depth groups (catalogue from Barberi et al., 2022; Ferrari et al., 2024). (3) Petrological data, expressed as the CaO/Al_2O_3 ratio in glass, reflect temporal changes in magma composition and differentiation; higher ratios indicate more primitive magma, while lower ratios denote more evolved compositions (from Corsaro et al., 2024). Orange shaded bands correspond to paroxysmal sequences 1 and 2

549 The clusters of deep earthquakes at 10–30 km b.s.l., particularly those in June, October, and
550 December 2020 and January 2021 (Fig. 13), precede or coincide with marked increases in CaO/Al_2O_3
551 ratios, suggesting the arrival of more primitive magma batches from depth. This temporal association
552 supports the interpretation that episodes of deep seismicity represent the ascent of new, less-evolved
553 magma, which upon reaching shallower levels and mixing with resident evolved magma drives the
554 observed compositional variability in erupted products at Etna.
555
556 Based on this integrated analysis, we defined the modelling phases for the pre-paroxysmal period,
557 PreSEQ(a) and PreSEQ(b), with PreSEQ(a) ranging from May to October 2020 and PreSEQ(b) from
558 October 2020 to mid-February 2021. These phases allow us to characterise the sources of the
559 observed deformation patterns during the pre-paroxysmal period that exhibited distinct responses to
560 different levels of Etna's plumbing system. This period remains challenging to model, since the
561 observed deformation reveals a superposition of multiple interacting processes, including magma
562 intrusions at different depths, gas pressure dynamics, structural modifications because of lateral
563 sliding, and potential coupling between shallow and intermediate magmatic systems.

564 **Distinct dynamics of the paroxysmal sequences**
565 Paroxysmal activity began in December 2020 with three lava fountains and intensified with the onset
566 of the paroxysmal Sequence 1 on 16 February 2021. The larger volumes of erupted material and the
567 high magma-supply rate during this sequence produced rapid pressure changes in the plumbing
568 system (Proietti et al., 2023), and the resulting deflation observed during this sequence can be
569 attributed to depressurisation of a shallow reservoir located at a depth of approximately 3.7 km b.s.l.,
570 as indicated by the deformation modelling (Table 2). The deformation pattern appears directly
571 controlled by the balance between magma input and withdrawal: while during the pre-paroxysmal
572 period the horizontal component of the displacement was larger than the vertical component, during
573 paroxysmal deflation the vertical component became dominant, producing clear and consistent
574 subsidence patterns. This shift is consistent with the asymmetry between inflation and deflation
575 documented at Mount Etna, where pressurisation-driven spreading is largely accommodated by non-
576 elastic deformation along fault systems, which prevents the flank spreading that occurs during
577 inflation from being fully recovered during subsequent deflation phases (Bonforte et al., 2008),
578 leaving a residual deformation signature in the edifice.
579
580 Between the two paroxysmal sequences (1 April to 19 May 2021), a small inflation of about 1 cm at
581 summit GNSS stations suggests renewed pressurisation. Corsaro et al. (2024) proposed that during
582 this interval magma was stored in the shallow reservoir, followed by progressive cooling and

583 crystallisation. While crystallisation alone tends to increase magma density, which would normally
584 drive a subsidence signal at the surface (Parker et al., 2014), the observed slight inflation indicates
585 the involvement of an additional mechanism. Observational and experimental studies show that when
586 volatile exsolution accompanies crystallisation (a process known as second boiling), the expansion
587 of exsolved gases can generate net inflation. Biondi et al. (2023), for example, reported that in Long
588 Valley Caldera a magma body emplaced at ~3–8 km depth generated uplift and seismicity without
589 evidence of new magma intrusion, attributing this to second boiling. Brookfield et al. (2023) similarly
590 identify crystallisation-driven volatile exsolution as a source of overpressure in volcanic systems. We
591 therefore interpret the observed slight summit inflation as evidence of *second-boiling*-induced
592 pressurisation. This process can increase reservoir overpressure, accelerate magma ascent and
593 increase eruptive explosivity (Cassidy et al., 2018), consistent with the type of activity observed
594 during the second paroxysmal sequence (Corsaro et al. 2024).
595
596 The pressurisation driven by second boiling, combined with renewed shallow magma input, likely
597 contributed to the conditions that preceded the onset of SEQ2. In contrast to SEQ1, whose
598 deformation is well reproduced by a single shallow source and is consistent with an equilibrated
599 input-output dynamic, SEQ2 displays more complex deformation patterns requiring a combination
600 of Yang- and Okada-type sources. This complexity suggests overlapping processes including
601 crystallisation, gas exsolution, shallow magma input, and renewed flank slip, and is consistent with
602 the larger modelling uncertainties obtained for this period.

603 **Comparison with erupted volumes and reservoir behaviour**
604 A notable discrepancy in the modelled deformation sources for the paroxysmal sequences lies in the
605 estimated volume change, which is smaller than values obtained in previous studies that used different
606 methods. The volumetric analysis of lava conducted by Proietti et al. (2023) indicates erupted lava
607 volumes of $(42 \pm 8) \times 10^6$ m³ during SEQ1 and $(29 \pm 6) \times 10^6$ m³ during SEQ2, suggesting a shift
608 toward a less voluminous eruptive period, and, consequently, weaker ground-deformation signals. In
609 contrast, our geodetic modelling indicates much smaller source volume changes, namely (7.3 ± 0.1)
610 $\times 10^6$ m³ during SEQ1 and $(7.2 \pm 0.4) \times 10^6$ m³ during SEQ2. Bonaccorso et al. (2021), for example,
611 estimated a total discharged volume of approximately 52.5×10^6 m³ during the paroxysmal SEQ1
612 based on strain variations. These discrepancies between geodetic volumes and eruptive volumes have
613 been documented in previous studies on volcanic eruptions (Mastin et al., 2008; Walder et al., 2008;
614 Voight et al., 2010; Wasser et al., 2021) and are often attributed to magma compressibility, whereby
615 the presence of an exsolved gas phase allows the magma to contract as pressure increases, diminishing
616 the surface displacement signal (Edmonds et al., 2019). Carbone et al. (2023) provide a joint analysis

of gravity and deformation data for a portion of SEQ2 (June–July 2021) and show that the expected contraction of the reservoir due to magma withdrawal was substantially reduced. They attribute this to a pressure drop in the reservoir that likely increased the amount of exsolved gas, thereby attenuating the reservoir contraction and producing smaller deformation signals. This suggests that a substantial fraction of the volumetric change associated with magma withdrawal was offset by the expansion of exsolved gases, leading to less pronounced deformation than would be expected from the erupted volumes alone. This mechanism is consistent with the second-boiling-induced pressurisation that likely occurred between SEQ1 and SEQ2.

Syn-eruptive recharge may also help explain the discrepancy. If fresh magma ascended from a deeper reservoir and entered the shallow system during the paroxysmal sequences, it would have partially refilled the chamber, compensating for eruption-driven deflation. Under this interpretation, the net geodetically observed ΔV underestimates the true volume loss from eruption alone. Petrological support for this mechanism comes from the more primitive compositions recorded in SEQ2 products, suggesting the involvement of deeper magma sources during this sequence, consistent with the recharge signal already identified in the pre-paroxysmal period (Corsaro et al., 2024).

Vertically stratified plumbing system

De Gori et al. (2021) applied time-lapse tomography based on seismicity recorded at Mt. Etna between December 2019 and February 2021 and identified fresh magma accumulating in three distinct reservoirs at different depths within the central plumbing system: a main reservoir between 3 and 9 km depth that serves as the primary accumulation zone and two shallower reservoirs at approximately −1 km and 1 km depth beneath the summit craters, where fresh magma rising from the deep reservoir briefly accumulates before feeding lava fountains and summit eruptive activity. These shallower reservoirs are beyond the detection capability of the geodetic datasets used in this study, as GNSS coverage near the summit is limited by sparse station density in this sector, while InSAR coherence is degraded by steep topography, atmospheric artefacts, and thick pyroclastic deposits continuously deposited during paroxysmal activity.

The deformation sources obtained from the geodetic modelling in this study are consistent with the main magma reservoir region found by De Gori et al. (2021). During the pre-paroxysmal period, the deformation sources are located beneath the summit area at depths between 5.5 and 4.3 km b.s.l., coinciding with the intermediate and vertical elongated main reservoir identified by De Gori et al. (2021). Figure 14 shows a schematic vertical W–E cross-section of Mt. Etna across the summit area, illustrating the position of the modelled sources derived from GNSS data for the pre-paroxysmal

period and from SISTEM-derived displacement for the two paroxysmal sequences. The underlying P-wave velocity (Vp) structure from seismic tomography (data provided by De Gori et al., 2021) highlights zones of lower seismic velocity (red shading), interpreted as regions of partial melt and/or recent magma intrusion.

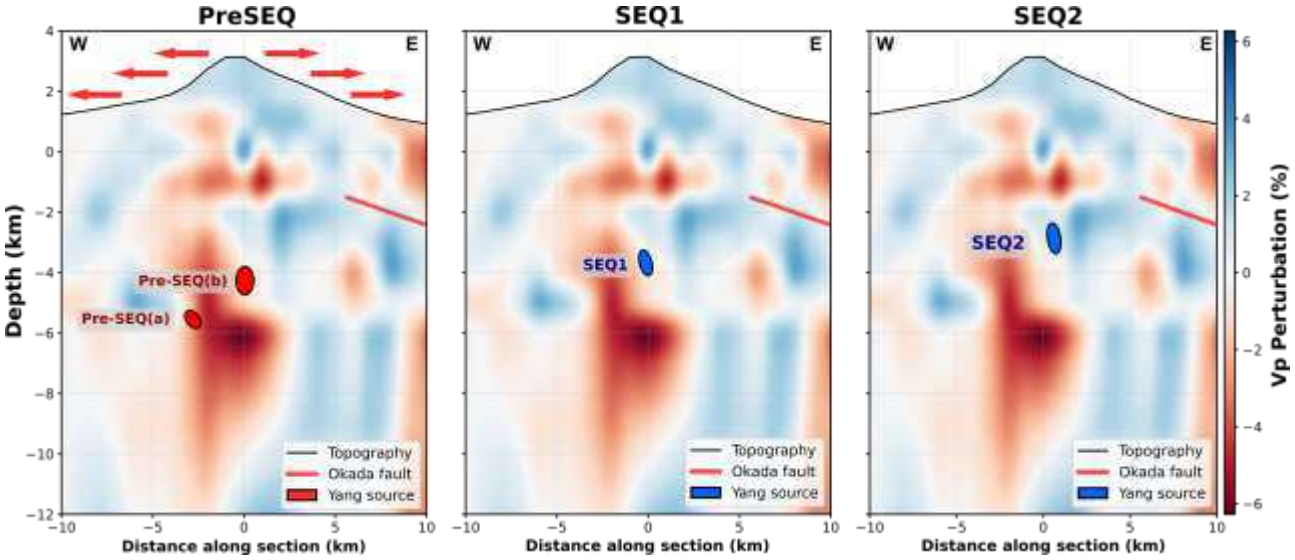


Fig. 14 Schematic vertical W-E cross-section of Mt. Etna across the summit area, showing the position of the modelled sources derived from GNSS data for the pre-paroxysmal period (left) and from SISTEM-derived displacement for the two paroxysmal sequences (SEQ1 and SEQ2; middle and right, respectively). For the pre-paroxysmal period, two distinct sources are displayed, corresponding to two sub-periods defined based on variations detected in the geodetic observations. The Okada dislocation plane is shown at the modelled position representing cumulative eastern flank motion. Underlying P-wave velocity (Vp) structure from seismic tomography (data provided by De Gori et al., 2021) highlights zones of lower seismic velocity (red shading), interpreted as regions of partial melt and/or recent magma intrusion

During the paroxysmal sequences, the sources shift to shallower depths, between 3.7 km and 2.9 km b.s.l. This spatial and temporal evolution of the deformation sources indicates progressive upward magma migration from a deeper reservoir or staging chamber toward the shallow plumbing system as paroxysmal activity approached. This may also suggest that the shallower sources during the paroxysmal sequences represent the active conduit system that directly feeds the paroxysmal activity, while the deeper pre-paroxysmal sources reflect pressurization and magma accumulation in the main reservoir prior to ascent.

Together, these observations support the interpretation of Etna's plumbing system as a vertically stratified and dynamically connected reservoir network, where magma migrates stepwise from deeper storage regions to shallower levels. The temporal evolution of the deformation sources is therefore consistent with a structured ascent pathway, in which pre-paroxysmal pressurisation at depth transitions into shallow reservoir activity that culminates in paroxysmal eruptions.

The Okada dislocation source inferred from the pre-paroxysmal period is located at a depth of approximately 1.5 km b.s.l. In Fig. 14, this source, represented by the inclined red line on the eastern side, aligns closely with the boundary between the low Vp zone (red), interpreted as a mechanically weak layer, and the higher Vp zone (blue), consistent with a detachment surface localised at a pre-existing rheological boundary imaged by seismic tomography. The location of this source suggests that the fault plane is structurally controlled by this boundary, which may represent a pre-existing weakness zone that facilitates slip.

Conclusions

In this study, we analysed ground deformation associated with the 2020–2022 paroxysmal activity at Mount Etna through joint analysis of InSAR and GNSS data, integrated using the SISTEM approach to reconstruct 3D displacement fields. We used analytical modelling to constrain the geometry, depth and volume changes of the deformation sources during the paroxysmal sequences SEQ1 and SEQ2 and the pre-paroxysmal period. We also included complementary seismic and petrological datasets to interpret the deformation sources and their magmatic drivers.

The pre-paroxysmal period was characterised by early and sustained deformation, including accelerating eastward motion of the eastern flank and repeated clusters of deep and intermediate-depth seismicity. Petrological evidence of progressively more primitive magma compositions supports the interpretation that fresh magma was introduced at depth beginning in mid-2020. Geodetic inversions reveal upward migration of pressurised sources from ~5.5 km to ~4.2 km depth, indicating progressive pressurisation of the intermediate plumbing system, while deflation sources associated with the paroxysmal sequences are situated at shallower depths between 3.7 km and 2.9 km b.s.l., in agreement with previous geodetic studies of Etna's shallow plumbing system (e.g. Palano et al., 2024). The temporal alignment of deep seismicity, compositional shifts toward more primitive magmas, and geodetic source migration provides strong evidence for episodic, vertically stratified magma recharge, consistent with a dynamically connected plumbing system in which magma migrated stepwise from deeper reservoirs to shallower levels before culminating in paroxysmal activity. The dominant deformation pattern during the pre-paroxysmal period reflects both magmatic pressurisation and flank instability, supporting a mechanically coupled system in which magma input weakened the sedimentary basement, accelerated lateral flank motion, and modified stress conditions within the central edifice, processes that directly influenced the timing and character of the subsequent paroxysmal sequences.

Paroxysmal Sequence 1, characterised by high magma supply and large eruptions (Corsaro et al., 2024), produced a volcano-wide centripetal deformation field consistent with a system in equilibrium between magma input and output, where rapid withdrawal from a shallow reservoir drove pronounced deflation sufficiently intense to temporarily mask Etna's characteristic eastward flank motion. In contrast, Sequence 2, with lower magma supply and smaller eruptions, exhibited reduced deflation intensity and larger source model uncertainties, reflecting the greater complexity of processes active at the onset of this sequence, including crystallisation, volatile exsolution through second boiling, and persistent flank slip. The contrasting deformation signatures of the two sequences, produced by the same volcanic system within months of each other, illustrate how strongly Etna's eruptive character is modulated by evolving shallow storage conditions.

Integrating complementary seismic and petrological datasets with our geodetic analysis provided stronger constraints on the conceptual model of the observed volcanic processes and their associated deformation sources, which geodetic analysis alone cannot fully resolve. Taken together, our results show that the 2020–2022 paroxysmal cycle was driven by stepwise magma ascent from deep reservoirs to shallow levels, strongly modulated by flank kinematics and evolving storage conditions. The geodetic network recorded the onset of this recharge episode earlier than both the deep seismic response and the magma's geochemical signature, highlighting the value of continuous GNSS monitoring in tracking the earliest stages of magmatic recharge at continuously active volcanoes.

References

Acocella, V., & Neri, M. (2003). What makes flank eruptions? The 2001 Etna eruption and its possible triggering mechanisms. *Bulletin of Volcanology, 65*(6), 517–529.

Acocella, V., Neri, M., & Norini, G. (2013). An overview of experimental models to understand a complex volcanic instability: Application to Mount Etna, Italy. *Journal of volcanology and geothermal research*, *251*, 98-111.

Acocella, V., Neri, M., Behncke, B., Bonforte, A., Del Negro, C., & Ganci, G. (2016). Why does a mature volcano need new vents? The case of the New Southeast Crater at Etna. *Frontiers in Earth Science*, *4*, 67.

Aiuppa, A., Moretti, R., Federico, C., Giudice, G., Gurrieri, S., Liuzzo, M., ... & Valenza, M. (2007). Forecasting Etna eruptions by real-time observation of volcanic gas composition. *Geology*, *35*(12), 1115-1118.

Aiuppa, A., Bitetto, M., Delle Donne, D., La Monica, F. P., Tamburello, G., Coppola, D., ... & Ripepe, M. (2021). Volcanic CO2 tracks the incubation period of basaltic paroxysms. *Science advances*, *7*(38), eabh0191.

Aiuppa, A., Lo Bue Trisciuzzi, G., Alparone, S., Bitetto, M., Coltelli, M., Delle Donne, D., ... & Pecora, E. (2023). A SO2 flux study of the Etna volcano 2020–2021 paroxysmal sequences. *Frontiers in Earth Science*, *11*, 1115111.

Akaike, H. (1974) A New Look at the Statistical Model Identification. *IEEE Transactions on Automatic Control*, AC- 19, 716-723.

Aloisi, M., Bonaccorso, A., Cannavò, F., & Currenti, G. M. (2018). Coupled short-and medium-term geophysical signals at Etna volcano: Using deformation and strain to infer magmatic processes from 2009 to 2017. *Frontiers in Earth Science*, *6*, 109.

Aloisi, M., Bonaccorso, A., Cannavò, F., Currenti, G., & Gambino, S. (2020). The 24 December 2018 eruptive intrusion at Etna volcano as revealed by multidisciplinary continuous deformation networks (CGPS, borehole strainmeters, and tiltmeters). *Journal of Geophysical Research: Solid Earth, 125*(8), e2019JB019117.

Alparone, S., Barberi, G., Cocina, O., Giampiccolo, E., Musumeci, C., and Patanè, D. (2012). Intrusive mechanism of the 2008–2009 Mt. Etna eruption: Constraints by tomographic images and stress tensor analysis. *Journal of Volcanology and Geothermal Research*, 229:50–63.

Alparone, S., Bonaccorso, A., Bonforte, A., & Currenti, G. (2013). Long-term stress-strain analysis of volcano flank instability: The eastern sector of Etna from 1980 to 2012. *Journal of Geophysical Research: Solid Earth*, *118*(9), 5098-5108.

Andronico, D., Scollo, S., and Cristaldi, A. (2015). Unexpected hazards from tephra fallouts at Mt Etna: The 23 November 2013 lava fountain. *Journal of Volcanology and Geothermal Research*, 304:118–125.

771 Andronico, D., Cannata, A., Di Grazia, G., & Ferrari, F. (2021). The 1986–2021 paroxysmal episodes
772 at the summit craters of Mt. Etna: Insights into volcano dynamics and hazard. *Earth-Science Reviews,*
773 *220*, 103686.

774 Apuani, T., Corazzato, C., Merri, A., & Tibaldi, A. (2013). Understanding Etna flank instability
775 through numerical models. *Journal of volcanology and geothermal research*, *251*, 112-126.

776 Bagagli, M., Montagna, C. P., Papale, P., & Longo, A. (2017). Signature of magmatic processes in
777 strainmeter records at Campi Flegrei (Italy). *Geophysical Research Letters, 44*(2), 718–725.

778 Bagnardi, M., & Hooper, A. (2018). Inversion of surface deformation data for rapid estimates of
779 source parameters and uncertainties: A Bayesian approach. *Geochemistry, Geophysics, Geosystems,*
780 *19*(7), 2194–2211.

781 Barberi G. et al. (2022). La sismicità dell'area etnea nel periodo gennaio – dicembre 2020, Quad.
782 Geofis., 179: 1-30. https://doi.org/10.13127/qdg/179

783 Bato, M., Lundgren, P., Pinel, V., Solidum Jr, R., Daag, A., & Cahulogan, M. (2021). The 2020
784 eruption and large lateral dike emplacement at Taal volcano, Philippines: Insights from satellite radar
785 data. *Geophysical Research Letters, 48*(7), e2021GL092803.

786 Behncke, B. and Neri, M. (2003). The July–August 2001 eruption of Mt. Etna (Sicily). *Bulletin of*
787 *Volcanology*, 65(7):461–476.

788 Behncke, B., Branca, S., Corsaro, R. A., De Beni, E., Miraglia, L., & Proietti, C. (2014). The 2011–
789 2012 summit activity of Mount Etna: Birth, growth and products of the new SE crater. *Journal of*
790 *Volcanology and Geothermal Research*, *270*, 10-21.

791 Bertiger, W., Bar-Sever, Y., Dorsey, A., Haines, B., Harvey, N., Hemberger, D., ... *et al.* (2020).
792 GIPSYX/RTGX, a new tool set for space geodetic operations and research. *Advances in Space*
793 *Research, 66*(3), 469–489.

794 Biggs, J., Ebmeier, S., Aspinall, W., Lu, Z., Pritchard, M., Sparks, R., & Mather, T. (2014). Global
795 link between deformation and volcanic eruption quantified by satellite imagery. *Nature*
796 *Communications, 5*(1), 3471.

797 Biondi, E., Zhu, W., Li, J., Williams, E. F., & Zhan, Z. (2023). An upper-crust lid over the Long
798 Valley magma chamber. Science Advances, 9(42), eadi9878.

799 Bonaccorso, A., Bonforte, A., Guglielmino, F., Palano, M., & Puglisi, G. (2006). Composite ground
800 deformation pattern forerunning the 2004–2005 Mount Etna eruption. *Journal of Geophysical*
801 *Research: Solid Earth*, *111*(B12).

802 Bonaccorso, A., Currenti, G., Linde, A., & Sacks, S. (2013). New data from borehole strainmeters to
803 infer lava fountain sources (Etna 2011–2012). *Geophysical Research Letters*, *40*(14), 3579-3584.

804 Bonaccorso, A., Calvari, S., Linde, A., & Sacks, S. (2014). Eruptive processes leading to the most
805 explosive lava fountain at Etna volcano: The 23 November 2013 episode. Geophysical Research
806 Letters, 41(14), 4912-4919.

807 Bonaccorso, A. and Calvari, S. (2017). A new approach to investigate an eruptive paroxysmal
808 sequence using camera and strainmeter networks: Lessons from the 3–5 December 2015 activity at
809 Etna volcano. *Earth and Planetary Science Letters*, 475:231–241.

810 Bonaccorso, A., & Aloisi, M. (2021). Tracking magma storage: New perspectives from 40 years
811 (1980–2020) of ground deformation source modeling on etna volcano. *Frontiers in Earth Science*, 9,
812 638742.

813 Bonaccorso, A., Carleo, L., Currenti, G., & Sicali, A. (2021). Magma migration at shallower levels
814 and lava fountains sequences as revealed by borehole dilatometers on Etna volcano. *Frontiers in*
815 *Earth Science, 9*, 740505.

816 Bonforte, A., & Puglisi, G. (2003). Magma uprising and flank dynamics on Mount Etna volcano,
817 studied using GPS data (1994–1995). *Journal of Geophysical Research: Solid Earth*, *108*(B3).

818 Bonforte, A., & Puglisi, G. (2006). Dynamics of the eastern flank of Mt. Etna volcano (Italy)
819 investigated by a dense GPS network. *Journal of Volcanology and Geothermal Research*, *153*(3-4),
820 357-369.

821 Bonforte, A., Bonaccorso, A., Guglielmino, F., Palano, M., and Puglisi, G. (2008). Feeding system
822 and magma storage beneath Mt. Etna as revealed by recent inflation/deflation cycles. Journal of
823 Geophysical Research: Solid Earth, 113(B5).

824 Bonforte, A., Gambino, S., & Neri, M. (2009). Intrusion of eccentric dikes: The case of the 2001
825 eruption and its role in the dynamics of Mt. Etna volcano. *Tectonophysics, 471*(1-2), 78–86.

826 Bonforte, A., Guglielmino, F., Coltelli, M., Ferretti, A., and Puglisi, G. (2011). Structural assessment
827 of Mount Etna volcano from Permanent Scatterers analysis. Geochemistry, Geophysics, Geosystems,
828 12(2).

829 Bonforte, A., Carnazzo, A., Gambino, S., Guglielmino, F., Obrizzo, F., & Puglisi, G. (2013). A
830 multidisciplinary study of an active fault crossing urban areas: The Trecastagni Fault at Mt. Etna
831 (Italy). *Journal of volcanology and geothermal research*, *251*, 41-49.

832 Bonforte, A., Guglielmino, F., & Puglisi, G. (2019). Large dyke intrusion and small eruption: The
833 December 24, 2018 Mt. Etna eruption imaged by Sentinel-1 data. *Terra Nova, 31*(4), 405–412.

834 Bonforte, A., Cannavò, F., Gambino, S., & Guglielmino, F. (2021). Combining high- and low-rate
835 geodetic data analysis for unveiling rapid magma transfer feeding a sequence of violent summit
836 paroxysms at Etna in late 2015. *Applied Sciences, 11*(10), 4630.

837 Borgia, A., Ferrari, L., and Pasquarè, G. (1992). Importance of gravitational spreading in the tectonic
838 and volcanic evolution of Mount Etna. *Nature*, 357(6375):231–235.

839 Borgia, A., Lanari, R., Sansosti, E., Tesauro, M., Berardino, P., Fornaro, G., Neri, M., and Murray,
840 J. (2000a). Actively growing anticlines beneath Catania from the distal motion of Mount Etna's
841 decollement measured by SAR interferometry and GPS. *Geophysical Research Letters*, 27(20):3409–
842 3412.

843 Branca, S., & Del Carlo, P. (2004). Eruptions of Mt. Etna during the past 3,200 years: A revised
844 compilation integrating the historical and stratigraphic records. *Mt. Etna: Volcano Laboratory*.

Brookfield, A., Cassidy, M., Weber, G., Popa, R. G., Bachmann, O., & Stock, M. J. (2023). Magmatic volatile content and the overpressure 'sweet spot': Implications for volcanic eruption triggering and style. *Journal of Volcanology and Geothermal Research*, *444*, 107916.

Bruno, V., Aloisi, M., Gambino, S., Mattia, M., Ferlito, C., & Rossi, M. (2022). The most intense deflation of the last two decades at Mt. Etna: The 2019–2021 evolution of ground deformation and modelled pressure sources. *Geophysical Research Letters, 49*(6), e2021GL095195.

Calvari, S., Bilotta, G., Bonaccorso, A., Caltabiano, T., Cappello, A., Corradino, C., ... *et al.* (2020). The VEI 2 Christmas 2018 Etna eruption: A small but intense eruptive event or the starting phase of a larger one? *Remote Sensing, 12*(6), 905.

Calvari, S., Biale, E., Bonaccorso, A., Cannata, A., Carleo, L., Currenti, G., ... *et al.* (2022). Explosive paroxysmal events at Etna volcano of different magnitude and intensity explored through a multidisciplinary monitoring system. *Remote Sensing, 14*(16), 4006.

Calvari, S. and Nunnari, G. (2022). Comparison between automated and manual detection of lava fountains from fixed monitoring thermal cameras at Etna Volcano, Italy. *Remote Sensing*, 14(10):2392.

Cannata, A., Giudice, G., Gurrieri, S., Montalto, P., Alparone, S., Di Grazia, G., ... & Liuzzo, M. (2010). Relationship between soil CO2 flux and volcanic tremor at Mt. Etna: implications for magma dynamics. *Environmental Earth Sciences*, *61*(3), 477-489.

Cannata, A., Spedalieri, G., Behncke, B., Cannavò, F., Di Grazia, G., Gambino, S., ... Palano, M. (2015). Pressurization and depressurization phases inside the plumbing system of Mount Etna volcano: Evidence from a multiparametric approach. *Journal of Geophysical Research: Solid Earth, 120*(9), 5965–5982.

Cannata, A., Di Grazia, G., Giuffrida, M., Gresta, S., Palano, M., Sciotto, M., ... & Zuccarello, F. (2018). Space-time evolution of magma storage and transfer at Mt. Etna Volcano (Italy): the 2015–2016 Reawakening of Voragine Crater. *Geochemistry, Geophysics, Geosystems*, 19(2), 471-495.

Cannavò, F. (2019). A new user-friendly tool for rapid modelling of ground deformation. *Computers & Geosciences*, *128*, 60-69.

Cannavò, F., Sciotto, M., Cannata, A., and Di Grazia, G. (2019). An integrated geophysical approach to track magma intrusion: The 2018 Christmas Eve eruption at Mount Etna. *Geophysical Research Letters*, 46(14):8009–8017.

Carleo, L., Currenti, G., & Bonaccorso, A. (2023). Clustering of eruptive events from high-precision strain signals recorded during the 2020–2022 lava fountains at the Etna volcano (Italy). *Natural Hazards and Earth System Sciences, 23*(5), 1743–1754.

Carrère, L., Lyard, F., Cancet, M., Guillot, A., & Picot, N. (2016). Finite element solution FES2014: A new tidal model—validation results and perspectives for improvements. Presented at ESA Living Planet Conference, Prague.

Cassidy, M., Manga, M., Cashman, K., & Bachmann, O. (2018). Controls on explosive-effusive volcanic eruption styles. *Nature communications*, *9*(1), 2839.

Chen, C. W., & Zebker, H. A. (2000). Network approaches to two-dimensional phase unwrapping: Intractability and two new algorithms. *Journal of the Optical Society of America A, 17*(3), 401–414.

Corsaro, R., Di Renzo, V., Distefano, S., Miraglia, L., & Civetta, L. (2013). Relationship between petrologic processes in the plumbing system of Mt. Etna and the dynamics of the eastern flank from 1995 to 2005. *Journal of Volcanology and Geothermal Research, 251*, 75–89.

Corsaro, R. A., Andronico, D., Behncke, B., Branca, S., Caltabiano, T., Ciancitto, F., ... & Spata, G. (2017). Monitoring the December 2015 summit eruptions of Mt. Etna (Italy): Implications on eruptive dynamics. *Journal of Volcanology and Geothermal Research*, *341*, 53-69.

Corsaro, R. A., & Miraglia, L. (2022). Near real-time petrologic monitoring on volcanic glass to infer magmatic processes during the February–April 2021 paroxysms of the South-East crater, Etna. *Frontiers in Earth Science, 10*, 828026.

Corsaro, R. A., Miraglia, L., Arienzo, I., & Di Renzo, V. (2024). The 2020–2022 paroxysmal episodes of the South-East Crater (Mt. Etna): insights into high-frequency eruptive activity from petrological monitoring. *Bulletin of Volcanology*, *86*(10), 85.

De Beni, E., Proietti, C., Cantarero, M., Greco, F., Mirabella, L. T., Messina, A., ... & Vajda, P. (2026). The dynamic summer of 2024 at Mt. Etna documented by UAS: Morphological changes and their gravimetric effects. *Journal of Volcanology and Geothermal Research*, *472*, 108562.

De Gori, P., Giampiccolo, E., Cocina, O., Branca, S., Doglioni, C., & Chiarabba, C. (2021). Re-pressurized magma at Mt. Etna, Italy, may feed eruptions for years. *Communications Earth & Environment*, *2*(1), 216.

Doin, M. P., Lasserre, C., Peltzer, G., Cavalié, O., & Doubre, C. (2009). Corrections of stratified tropospheric delays in SAR interferometry: Validation with global atmospheric models. *Journal of Applied Geophysics*, *69*(1), 35-50.

Dzurisin, D. (2006). *Volcano deformation: New geodetic monitoring techniques*. Springer Science & Business Media.

Edmonds, M., Cashman, K. V., Holness, M., & Jackson, M. (2019). Architecture and dynamics of magma reservoirs. *Philosophical Transactions of the Royal Society A: Mathematical, Physical and Engineering Sciences*, 377(2139).

Fattahi, H., Agram, P., & Simons, M. (2016). A network-based enhanced spectral diversity approach for TOPS time-series analysis. *IEEE Transactions on Geoscience and Remote Sensing, 55*(2), 777–786.

Ferrari F. et al. (2024). La sismicità dell'area etnea nel periodo Gennaio – Dicembre 2021, Quad. Geofis., 192: 1-32. https://doi.org/10.13127/qdg/192

Firetto Carlino, M., Lo Bue, R., Taroni, M., Coltelli, M., Cannavò, F., Cocina, O., Barberi, G., and Scarfì, L. (2025). Earthquake frequency-magnitude distribution at Mount Etna sheds light on magma ascent in the volcano's plumbing system. *Science Advances*, 11(41):eadx9873.

Freymueller, J. T., Murray, J. B., Rymer, H., & Locke, C. A. (2015). Ground deformation, gravity, and magnetics. In *The Encyclopedia of Volcanoes* (pp. 1101–1123). Elsevier.

Giuffrida, M., Cardone, M., Zuccarello, F., & Viccaro, M. (2023). Etna 2011–2022: Discoveries from a decade of activity at the volcano. *Earth-Science Reviews*, 104563.

Giuffrida, M., Scandura, M., Costa, G., Zuccarello, F., Sciotto, M., Cannata, A., & Viccaro, M. (2021). Tracking the summit activity of Mt. Etna volcano between July 2019 and January 2020 by integrating petrological and geophysical data. *Journal of Volcanology and Geothermal Research, 418*, 107350.

Goldstein, R. M., & Werner, C. L. (1998). Radar interferogram filtering for geophysical applications. *Geophysical Research Letters, 25*(21), 4035–4038.

Guglielmino, F., Nunnari, G., Puglisi, G., & Spata, A. (2011). Simultaneous and integrated strain tensor estimation from geodetic and satellite deformation measurements to obtain three-dimensional displacement maps. *IEEE Transactions on Geoscience and Remote Sensing, 49*(6), 1815–1826.

Gurrieri, S., Liuzzo, M., & Giudice, G. (2008). Continuous monitoring of soil CO2 flux on Mt. Etna: The 2004–2005 eruption and the role of regional tectonics and volcano tectonics. *Journal of Geophysical Research: Solid Earth*, *113*(B9).

Heap, M. J., Mollo, S., Vinciguerra, S., Lavallée, Y., Hess, K. U., Dingwell, D. B., ... & Iezzi, G. (2013). Thermal weakening of the carbonate basement under Mt. Etna volcano (Italy): implications for volcano instability. *Journal of volcanology and geothermal research*, *250*, 42-60.

Heap, M. J., & Violay, M. E. (2021). The mechanical behaviour and failure modes of volcanic rocks: a review. *Bulletin of Volcanology*, *83*(5), 33.

Inguaggiato, S., Vita, F., Cangemi, M., & Calderone, L. (2020). Changes in CO2 soil degassing style as a possible precursor to volcanic activity: The 2019 case of Stromboli paroxysmal eruptions. *Applied Sciences*, *10*(14), 4757.

INGV-OE (2020) Bollettini Settimanali sul monitoraggio vulcanico, geochimico e sismico del vulcano Etna. Available at: https:// www.ct.ingv.it/index.php/monitoraggio-esorveglianza/prodottidel-monitoraggio/bollettini-settimanalimultidisciplinari

INGV-OE (2021) Bollettini Settimanali sul monitoraggio vulcanico, geochimico e sismico del vulcano Etna. Available at: https:// www.ct.ingv.it/index.php/monitoraggio-esorveglianza/prodottidel-monitoraggio/bollettini-settimanalimultidisciplinari

Kouba, J. (2008). Implementation and testing of the gridded Vienna mapping function 1 (VMF1). *Journal of Geodesy, 82*(4), 193–205.

Lo Bue, R., Rappisi, F., Firetto Carlino, M., Giampiccolo, E., Cocina, O., Vanderbeek, B., & Faccenda, M. (2024). Crustal structure of Etna volcano (Italy) from P-wave anisotropic tomography. *Geophysical Research Letters, 51*(13), e2024GL108733.

Lundgren, P., Berardino, P., Coltelli, M., Fornaro, G., Lanari, R., Puglisi, G., ... Tesauro, M. (2003). Coupled magma chamber inflation and sector collapse slip observed with synthetic aperture radar interferometry on Mt. Etna volcano. *Journal of Geophysical Research: Solid Earth, 108*(B5).

957 Lundgren, P., Casu, F., Manzo, M., Pepe, A., Berardino, P., Sansosti, E., and Lanari, R. (2004).
958 Gravity and magma induced spreading of Mount Etna volcano revealed by satellite radar
959 interferometry. *Geophysical Research Letters*, 31(4).

960 Mastin, L. G., Roeloffs, E., Beeler, N. M., and Quick, J. E. (2008). Constraints on the size,
961 overpressure, and volatile content of the Mount St. Helens magma system from geodetic and dome-
962 growth measurements during the 2004-2006 eruption. *US Geol. Surv. Prof. Pap*, 1750:461–488.

963 Mattia, M., Bruno, V., Montgomery-Brown, E., Patanè, D., Barberi, G., & Coltelli, M. (2020).
964 Combined seismic and geodetic analysis before, during, and after the 2018 Mount Etna eruption.
965 *Geochemistry, Geophysics, Geosystems, 21*(9), e2020GC009218.

966 Métrich, N., Allard, P., Spilliaert, N., Andronico, D., & Burton, M. (2004). 2001 flank eruption of
967 the alkali- and volatile-rich primitive basalt responsible for Mount Etna's evolution in the last three
968 decades. *Earth and Planetary Science Letters, 228*(1-2), 1–17.

969 Mogi, K. (1958). Relations between the eruptions of various volcanoes and the deformation of the
970 ground surfaces around them. *Bulletin of the Earthquake Research Institute, 36*.

971 Murray, J. B., van Wyk de Vries, B., Pitty, A., Sargent, P., & Wooller, L. (2018). Gravitational sliding
972 of the Mt. Etna massif along a sloping basement. Bulletin of Volcanology, 80, 1-11.

973 Murray, J. B. (2019). The cryptic summit graben of Mt. Etna volcano. Journal of Volcanology and
974 Geothermal Research, 387, 106657.

975 Neri, M., & Acocella, V. (2006). The 2004–2005 Etna eruption: Implications for flank deformation
976 and structural behaviour of the volcano. *Journal of Volcanology and Geothermal Research*, *158*(1-
977 2), 195-206.

978 Neri, M., Casu, F., Acocella, V., Solaro, G., Pepe, S., Berardino, P., ... Lanari, R. (2009). Deformation
979 and eruptions at Mt. Etna (Italy): A lesson from 15 years of observations. *Geophysical Research*
980 *Letters*, 36(2).

981 Nunnari, G. and Puglisi, G. (1994). The global positioning system as a useful technique for measuring
982 ground deformations in volcanic areas. *Journal of Volcanology and Geothermal Research*, 61(3-
983 4):267–280.

984 Palano, M., Viccaro, M., Zuccarello, F., & Gresta, S. (2017). Magma transport and storage at Mt.
985 Etna (Italy): A review of geodetic and petrological data for the 2002–03, 2004 and 2006 eruptions.
986 *Journal of Volcanology and Geothermal Research*, 347, 149-164.

987 Palano, M., Calcaterra, S., Gambino, P., Porfidia, B., & Sparacino, F. (2023). GNSS-based long-term
988 deformation at Mount Etna volcano (Italy). *Results in Geophysical Sciences, 14*, 100056.

989 Palano, M., Pezzo, G., & Chiarabba, C. (2024). Magma budget, plutonic growth and lateral spreading
990 at Mt. Etna. *Communications Earth & Environment*, *5*(1), 95.

991 Parker, A. L., Biggs, J., & Lu, Z. (2014). Investigating long-term subsidence at Medicine Lake
992 Volcano, CA, using multitemporal InSAR. *Geophysical Journal International*, *199*(2), 844-859.

Pinel, V., Poland, M. P., & Hooper, A. (2014). Volcanology: Lessons learned from synthetic aperture radar imagery. *Journal of Volcanology and Geothermal Research, 289*, 81–113.

Poland, M. P., Peltier, A., Bonforte, A., & Puglisi, G. (2017). The spectrum of persistent volcanic flank instability: A review and proposed framework based on Kīlauea, Piton de la Fournaise, and Etna. *Journal of Volcanology and Geothermal Research*, *339*, 63-80.

Proietti, C., De Beni, E., Cantarero, M., Ricci, T., & Ganci, G. (2023). Rapid provision of maps and volcanological parameters: quantification of the 2021 Etna volcano lava flows through the integration of multiple remote sensing techniques. *Bulletin of Volcanology*, 85(10), 58.

Puglisi, G., Briole, P., & Bonforte, A. (2004a). Twelve years of ground deformation studies on Mt. Etna volcano based on GPS surveys. *Geophysical Monograph Series*, 143, 321-341.

Puglisi, G., & Bonforte, A. (2004b). Dynamics of Mount Etna Volcano inferred from static and kinematic GPS measurements. *Journal of Geophysical Research: Solid Earth*, *109*(B11).

Puglisi, G., Bonforte, A., Ferretti, A., Guglielmino, F., Palano, M., & Prati, C. (2008). Dynamics of Mount Etna before, during, and after the July–August 2001 eruption inferred from GPS and differential synthetic aperture radar interferometry data. *Journal of Geophysical Research: Solid Earth*, 113(B6).

Rosen, P. A., Gurrola, E., Sacco, G. F., & Zebker, H. (2012). The InSAR scientific computing environment. In *EUSAR 2012; 9th European Conference on Synthetic Aperture Radar* (pp. 730–733).

Scarfì, L., Barreca, G., Cassisi, C., & Langer, H. (2025). Earthquake clustering and structural modelling unravel volcano-tectonic complexity beneath Mount Etna. *Scientific Reports*, *15*(1), 18607.

Spampinato, L., Sciotto, M., Cannata, A., Cannavò, F., La Spina, A., Palano, M., ... & Caltabiano, T. (2015). Multiparametric study of the F ebruary–A pril 2013 paroxysmal phase of M t. E tna N ew S outh-E ast crater. Geochemistry, Geophysics, Geosystems, 16(6), 1932-1949.

Spilliaert, N., Allard, P., Métrich, N., & Sobolev, A. (2006). Melt inclusion record of the conditions of ascent, degassing, and extrusion of volatile-rich alkali basalt during the powerful 2002 flank eruption of Mount Etna (Italy). *Journal of Geophysical Research: Solid Earth, 111*(B4).

Tian, D., Uieda, L., Leong, W. J., Fröhlich, Y., Schlitzer, W., Grund, M., ... & Wessel, P. (2024). PyGMT: A Python interface for the Generic Mapping Tools-v0. 13.0.

Ubide, T., & Kamber, B. S. (2018). Volcanic crystals as time capsules of eruption history. *Nature Communications, 9*(1), 1–12.

Urlaub, M., Petersen, F., Gross, F., Bonforte, A., Puglisi, G., Guglielmino, F., ... & Kopp, H. (2018). Gravitational collapse of Mount Etna's southeastern flank. *Science Advances*, *4*(10), eaat9700.

Viccaro, M., Giacomoni, P. P., Ferlito, C., & Cristofolini, R. (2010). Dynamics of magma supply at Mt. Etna volcano (Southern Italy) as revealed by textural and compositional features of plagioclase phenocrysts. *Lithos, 116*(1-2), 77–91.

1029 Viccaro, M., Garozzo, I., Cannata, A., Di Grazia, G., & Gresta, S. (2014). Gas burst vs. gas-rich
1030 magma recharge: a multidisciplinary study to reveal factors controlling triggering of the recent
1031 paroxysmal eruptions at Mt. Etna. *Journal of volcanology and geothermal research*, *278*, 1-13.

1032 Voight, B., Widiwijayanti, C., Mattioli, G., Elsworth, D., Hidayat, D., and Strutt, M. (2010). Magma-
1033 sponge hypothesis and stratovolcanoes: Case for a compressible reservoir and quasi-steady deep
1034 influx at Soufrière Hills Volcano, Montserrat. *Geophysical Research Letters*, 37(19).

1035 Walder, J. S., Schilling, S. P., Vallance, J. W., and LaHusen, R. G. (2008). Effects of lava-dome
1036 growth on the Crater Glacier of Mount St. Helens, Washington. *Technical report, US Geological*
1037 *Survey*.

1038 Walter, T. R., Acocella, V., Neri, M., & Amelung, F. (2005). Feedback processes between magmatic
1039 events and flank movement at Mount Etna (Italy) during the 2002–2003 eruption. *Journal of*
1040 *Geophysical Research: Solid Earth, 110*(B10).

1041 Wasser, V. K., Lopez, T. M., Anderson, K. R., Izbekov, P. E., and Freymueller, J. T. (2021).
1042 Multidisciplinary constraints on magma compressibility, the pre-eruptive exsolved volatile fraction,
1043 and the H2O/CO2 Molar ratio for the 2006 Augustine eruption, Alaska. *Geochemistry, Geophysics,*
1044 *Geosystems*, 22(9):e2021GC009911.

1045 Wessel, P., Luis, J. F., Uieda, L. A., Scharroo, R., Wobbe, F., Smith, W. H., & Tian, D. (2019). The
1046 Generic Mapping Tools version 6. Geochemistry, Geophysics, Geosystems, 20*(11), 5556–5564.

1047 Yunjun, Z., Fattahi, H., & Amelung, F. (2019). Small baseline InSAR time series analysis:
1048 Unwrapping error correction and noise reduction. *Computers & Geosciences*, *133*, 104331.